nature immunology

Article

https://doi.org/10.1038/s41590-025-02386-2

Spatial patterning of fibroblast TGFβ signaling underlies treatment resistance in rheumatoid arthritis

Received: 11 March 2025

Accepted: 2 December 2025

Published online: 15 January 2026

Check for updates

A list of authors and their affiliations appears at the end of the paper

Treatment-refractory rheumatoid arthritis (RA) is a major unmet need, and the underlying mechanisms are poorly understood. To identify molecular determinants of refractory RA, we performed spatial transcriptomic profiling on synovial tissue biopsy samples taken 6 months before and after treatment. In the baseline biopsy samples of non-remitting patients, we identified increased fibrogenic signaling within vascular tissue niches, marked by high fibroblast *COMP* expression. We uncovered a role of endothelial-derived Notch signaling as an upstream regulator of fibroblast transforming growth factor beta (TGFβ) signaling via its opposing ability to induce TGFβ isoform expression while suppressing TGFβ receptors, generating a proximal-to-distal gradient of TGFβ sensitivity that can be altered with disruption of steady-state Notch signaling. In posttreatment biopsy samples, we observed significant immune depletion with expansion of fibrogenic niches, a process that can be reversed by inhibition of Notch and TGFβ signaling in RA patient-derived organoids. Collectively, our data implicate targeting of TGFβ signaling to prevent exuberant synovial tissue fibrosis as a potential therapeutic strategy for refractory RA.

Rheumatoid arthritis (RA) is a common autoimmune disease characterized by chronic inflammation in the synovium[1,2]. While there have been significant advances in the treatment of RA with the introduction of biologics targeting inflammatory mediators, treatment-refractory RA remains a major challenge[3]. Greater than 50% of patients do not achieve remission with initial lines of therapy and 5–30% of patients remain unresponsive to multiple lines[4,5]. Clinically, such treatment-refractory patients present more frequently with concomitant noninflammatory pain, suggesting an alternate pathophysiology[6]. However, the molecular mechanisms underlying refractory RA remain poorly understood. Synovial fibroblasts are mesenchymal cells that together with macrophages constitute the joint lining membrane[7]. In RA, fibroblasts undergo expansion and acquire pathological states that sustain inflammation and drive joint damage[8–12]. Transcriptomic analysis of RA synovium has revealed high phenotypic and functional diversity among synovial fibroblasts[8–11,13,14] and fibroblastic gene signatures that predict treatment failure[15–17].

Fibrosis is a pathogenic process characterized by exuberant fibroblast activation, leading to the accumulation of connective tissue components and extracellular matrix (ECM), mediated by TGFβ[18,19]. Fibrosis leading to organ damage is typically associated with autoimmune diseases such as systemic sclerosis and interstitial lung disease and is a contributor to joint stiffness and pain in osteoarthritis[20]. In contrast, the potential contribution of synovial tissue fibrosis to RA has not been well studied.

We have previously uncovered the role of spatial context in driving signals that generate fibroblast diversity and define positional identity[9,21]. Until recently, spatially aware transcriptomic profiling of fibroblasts required multiple iterations of protein or RNA detection, which poses a major barrier to high-dimensional characterization of cellular niches and associated signaling. Here, we applied a subcellular resolution, high-dimensional spatial transcriptomic technology to pretreatment and 6-month posttreatment synovial biopsy samples to identify spatial determinants of treatment resistance in recent-onset RA. At this stage, there is a window of opportunity to achieve remission, which predicts better outcomes[22]. In the baseline biopsy samples of non-remitting patients, we identified significant enrichment of

e-mail: kwei@bwh.harvard.edu

fibrogenic fibroblast signatures, marked by the expression of *COMP*, localized to vascular niches where we observed coordinated spatial patterning of TGFβ activity. Mechanistically, endothelial-derived Notch signaling actively fine-tunes TGFβ-mediated fibrogenic signaling by simultaneously inducing TGFβ expression and suppressing TGFβ receptor expression, resulting in the establishment of a perturbable endothelial proximal-to-distal transcriptional gradient among fibroblasts.

After treatment, both remission groups exhibited significant immune depletion; however, lack of pain-related clinical response sustained disease activity in non-remission patients, which was linked to increased fibrogenic signaling. Therapeutic inhibition of Notch and TGFβ signaling successfully reversed fibrogenic gene and protein expression in RA patient-derived synovial organoids. Together, these data suggest that TGFβ signaling drives an expansion of fibrogenic fibroblasts in RA that leads to a treatment-refractory synovial tissue phenotype and that targeting TGFβ signaling could represent an adjuvant therapy to prevent the development of refractory RA.

Results

Identification of distinct tissue niches in RA synovium

To identify spatial features associated with non-remission, we performed spatial transcriptomics analysis on 17 treatment-naive biopsy samples from patients with early RA as part of the 396.10 study (Fig. 1a). Newly diagnosed RA patients were assigned to triple-therapy disease-modifying antirheumatic drugs (DMARDs) or anti-tumor necrosis factor biologic adalimumab. Remission, defined as Disease Activity Score-28 for Rheumatoid Arthritis with Erythrocyte Sedimentation Rate (DAS28-ESR) < 2.6 and Disease Activity Score-28 for Rheumatoid Arthritis with C-reactive protein (DAS28-CRP) < 2.4, was recorded after 6 months of treatment (Supplementary Table 1). In this cohort, 10 patients achieved remission, 5 did not achieve remission and 2 patients, classified as borderline, met the criteria for only one of either DAS28-ESR or DAS28-CRP remission. Baseline DAS28-ESR/CRP and its individual components did not differ significantly between patients who achieved remission ($n = 10$) and those who did not ($n = 5$), but non-remitting patients had significantly lower improvements in disease activity (Supplementary Table 1). We first identified major synovial tissue niches in baseline biopsy samples using a method that leverages spatial differences in transcript expression to draw boundaries between tissue compartments[23] (Fig. 1b and Extended Data Fig. 1a). Graph-based clustering of tiles revealed seven niches that were enriched for distinct transcripts and their corresponding cell types: (1) fibroblast-rich, (2) vascular, (3) stromal-adipose, (4) lining fibroblasts ('liningF'), (5) lining macrophages ('liningM'), (6) T cells and B cells ('immuneT') and (7) plasma cells ('immuneP'; Fig. 1c,d, Extended Data Fig. 1a–c and Supplementary Table 1). The lining niches (liningF, liningM) consisted of a mix of synovial lining fibroblasts (*CD55*$^+$) and lining macrophages (*HTRA1*$^+$). The immune niches contained dense infiltrates composed of either primarily T cells (*CD3E*$^+$) and B cells (*MS4A1*$^+$; 'immuneT') or plasma cell aggregates (*MZB1*$^+$; 'immuneP'). Vascular niches consisted of various endothelial subtypes including venules (*SELP*$^+$), capillaries (*PLVAP*$^+$) and arterioles (*PODXL*$^+$), mural cells, including pericytes (*RGS5*$^+$) and vascular smooth cells (*ACTA2*$^+$) and *NOTCH3*$^+$ vascular fibroblasts. Stromal-adipose niches contained vascular cells and fibroblasts embedded among adipocytes (*ADIPOQ*$^+$). Fibroblast-rich niches were composed primarily of sublining fibroblasts (*COL6A1*^{hi}).

Hierarchical clustering of niche composition classified samples into three broad categories, one characterized by stromal-adipose enrichment ($n = 4$), another by immune niche enrichment ($n = 5$) and a third marked by expanded vascular and fibroblast niches ($n = 7$; Fig. 1c and Extended Data Fig. 1d). While we observed high concordance between immune niche tissue area and hematoxylin and eosin (H&E)-based lymphomyeloid pathotype classification[24] (Extended Data Fig. 1e), clear distinctions did not appear between the diffuse myeloid and pauci-immune pathotypes (Fig. 1c), suggesting that spatial transcriptomics analysis captures complexity in cellular organization beyond traditional histologic assessment of synovial tissue pathotype. Tissue areas of fibroblast-rich niches negatively correlated with the area of combined immune niches, consistent with prior studies utilizing histology[25,26] and single-cell transcriptomics[11,15,16] (Extended Data Fig. 1f). We observed no significant differences in baseline niche composition by remission status, although we could not exclude the possibility that heterogeneity in tissue sampling masked underlying distinctions (Extended Data Fig. 1g). Therefore, we investigated whether transcriptional differences could differentiate remission groups.

Elevated fibrogenic signatures in non-remission

Since the sample size of our cohort was limited, we leveraged bulk RNA-sequencing (RNA-seq) data from the larger PEAC cohort ($n = 69$)[16] to identify genes significantly associated with nonresponse (Fig. 2a). We applied the nonresponder gene signature to spatial niches and found enrichment of the signature in stromal-adipose, fibroblast-rich and vascular niches (Fig. 2b). Among synovial cell types, fibroblasts were enriched in the three nonresponder-associated niches and exhibited the highest nonresponse scores (Extended Data Fig. 2a).

To identify specific fibroblast phenotypes[15] most strongly associated with nonresponse, we subtyped fibroblasts in our spatial transcriptomic data and identified one lining and four sublining subsets. The fibrogenic sublining subset was characterized by high ECM gene expression (*COL6A1*, *COL8A1*, *COMP*), the inflammatory subset by expression of inflammatory mediators (*CXCL12*), and the vascular subset by *NOTCH3* and *THY1* expression. A minor subpopulation was marked by expression of *L1CAM*, a nerve-associated adhesion molecule[27] (Fig. 2c and Extended Data Fig. 2b). We confirmed that lining fibroblasts were the most abundant fibroblast subtype in lining niches and that vascular and inflammatory fibroblasts were most enriched in the immune niches (Fig. 2c)[28]. Notably, fibrogenic fibroblasts were the subtype most enriched for the nonresponse signature (Extended Data Fig. 2c) and were specifically expanded in the nonresponse-associated fibroblast-rich, stromal-adipose and vascular niches (Fig. 2c).

To assess whether fibrogenic programs stratified remission groups, we calculated a 12-gene fibrogenic activation score using fibrogenic fibroblast markers, including *POSTN*, *CTHRC1* and *SFRP4* previously described in fibrotic disease[29–31] (Fig. 2d and Extended Data Fig. 2d). The fibrogenic score was significantly elevated in pretreatment fibroblasts of non-remitting patients compared to remitting patients (Fig. 2d and Extended Data Fig. 2e,f).

While the vascular and inflammatory fibroblast compartments have previously been characterized[8,9,12,14], the fibrogenic compartment in RA remains incompletely understood[25]. To assess the phenotypic overlap between RA fibrogenic fibroblasts and myofibroblasts in fibrotic diseases, we first confirmed enrichment of the 12-gene fibrogenic fibroblast signature in publicly available systemic sclerosis and idiopathic pulmonary fibrosis datasets[32,33] (Extended Data Fig. 3a,b). Spatial profiling of RA synovial tissue and lung tissue from patients with late-stage RA interstitial lung disease (RA-ILD) exhibiting usual interstitial pneumonia (Extended Data Fig. 3c,d) then revealed high and specific enrichment of the signature in regions identified through histology as subepithelial-localized fibroblastic foci (Extended Data Fig. 3c). In RA synovial tissue, the fibrogenic signature was expressed more diffusely throughout the sublining compartment, with high-expressing regions characterized by deeper pink eosin staining compared to low-expressing regions, indicating increased ECM deposition. Collectively, we observed strong transcriptomic overlap between fibrogenic populations in RA and fibrotic disease (Extended Data Fig. 3d).

Next, to determine whether there are specific cellular subtypes within the RA fibrogenic compartment associated with nonresponse, we subsetted and reclustered fibroblasts from patients in the AMP RA/

https://doi.org/10.1038/s41590-025-02386-2

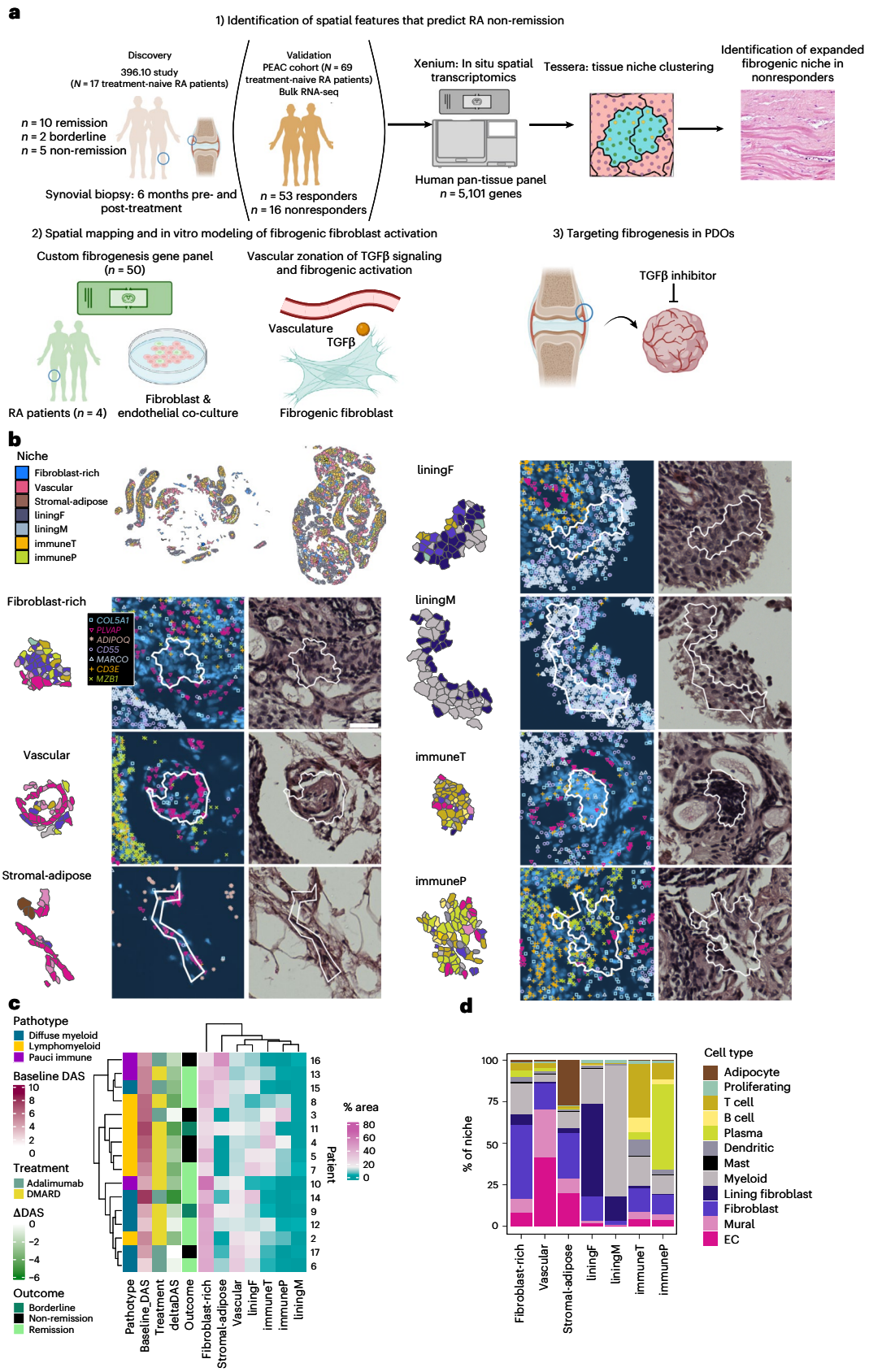

Fig. 1 | Identification of RA synovial tissue niches. a, Schematic overview of the study. **b**, Visualization of niches in a single synovial biopsy sample. Representative examples for each individual niche type with component cell types labeled are shown with corresponding DAPI and H&E images. Scale bar, 50 µm. **c**, Heat map representing the abundance of tissue niches, by tissue area, in each treatment-naive biopsy and the associated clinical metadata. Baseline DAS and ΔDAS represent the DAS28-ESR pretreatment and the change at 6 months, respectively. **d**, Stacked bar plot representing the proportion of cell types per niche. Schematic in **a** was created with BioRender.com.

https://doi.org/10.1038/s41590-025-02386-2

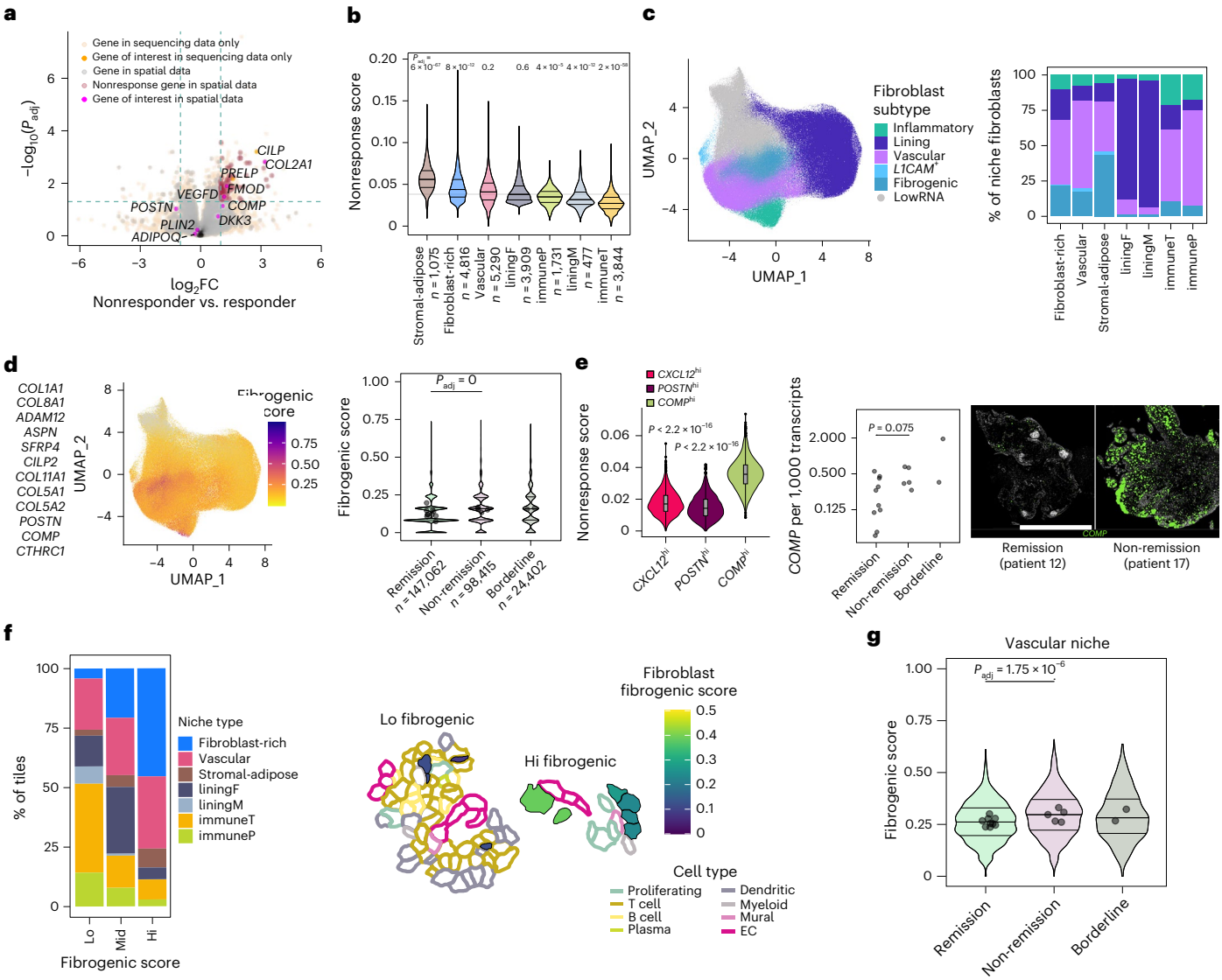

Fig. 2 | Fibrogenic signaling is enriched in non-remission biopsy samples. **a**, Volcano plot representing differentially expressed genes in nonresponders versus responders from bulk RNA-seq analysis of synovial tissue derived from treatment-naive patients. Genes in the upper-right quadrant are $\log_2$ fold change > 1 and $P_{adj} < 0.05$ between nonresponders and responders. Differential expression was tested with DESeq2 (negative-binomial generalized linear model (GLM); Wald test); *P* values are false discovery rate (FDR) corrected. Selected genes, including those in the nonresponder gene set, are highlighted. **b**, Violin plot representing the distribution of nonresponse scores per niche type, with the number of niches analyzed indicated. Statistical comparison by two-sided Wilcoxon test comparing a downsampled selection of nonresponse scores in 500 niches from each niche type to a random selection of scores from 500 other niches, with Bonferroni correction. Horizontal line represents the median nonresponse score across all niches analyzed. **c**, Uniform manifold approximation and projection (UMAP) plot of fibroblasts annotated by subtype, and stacked bar plot representing the proportion of each fibroblast subtype within each niche. **d**, UMAP (left) and violin plot (right) displaying the projection and distribution of single-cell fibrogenic U cell scores, respectively. Each dot in the violin plot represents the median fibrogenic score per patient, with signature genes indicated to the left of the UMAP. Statistical comparison by quasibinomial GLM with patient included as a cofactor, with Bonferroni correction across cell types. **e**, Violin plot (left) displaying the distribution of the nonresponder signatures ($n = 290$ genes) in $COMP^{hi}$, $POSTN^{hi}$ and $CXCL12^{hi}$ clusters, as calculated by UCell. Two-sided Wilcoxon test was used for statistical comparisons between the groups ($P < 2.2 \times 10^{-16}$ between $COMP^{hi}$ nonresponse score and each cluster). Jitter plot (right) representing quantification of normalized *COMP* transcript expression at baseline by remission status, with representative images of *COMP* transcript expression. Scale bar, 2 mm. Statistical comparison by two-sided Wilcoxon test. **f**, Stacked bar plot (left) representing the proportion of each niche type that had fibrogenic scores in the low ('lo'), medium ('mid') and high ('hi') categories with a representative example (right) of niche tiles that scored low and high for fibrogenic scores. **g**, Violin plot representing the distribution of fibrogenic scores for vascular niche tiles by remission status. Each dot represents the median per-patient fibrogenic score in vascular niches. Statistics calculated by two-sided GLM with patient as a cofactor, with FDR correction across niche types. The box plot in **e** shows the median and 25th–75th percentiles, the whiskers represent 1.5 times the interquartile range, and outliers are shown beyond the whiskers.

SLE single-cell RNA-sequencing (scRNA-seq) dataset[15] that were highly enriched for the 12-gene fibrogenic signature derived from the spatial transcriptomic dataset (top 10% of cells; Extended Data Fig. 4a). We observed three broad fibrogenic subclusters: a *CXCL12*-expressing inflammatory cluster, a *COMP*-expressing cluster that coexpressed *DKK3* and *FMOD*, previously found to be associated with treatment resistance[17], and a *POSTN*-expressing cluster relatively enriched for *COL1A1* expression, illustrating distinct phenotypes among RA fibrogenic fibroblasts (Extended Data Fig. 4b). Genes coexpressed in the $POSTN^{hi}$ cluster were positively associated with treatment response

https://doi.org/10.1038/s41590-025-02386-2

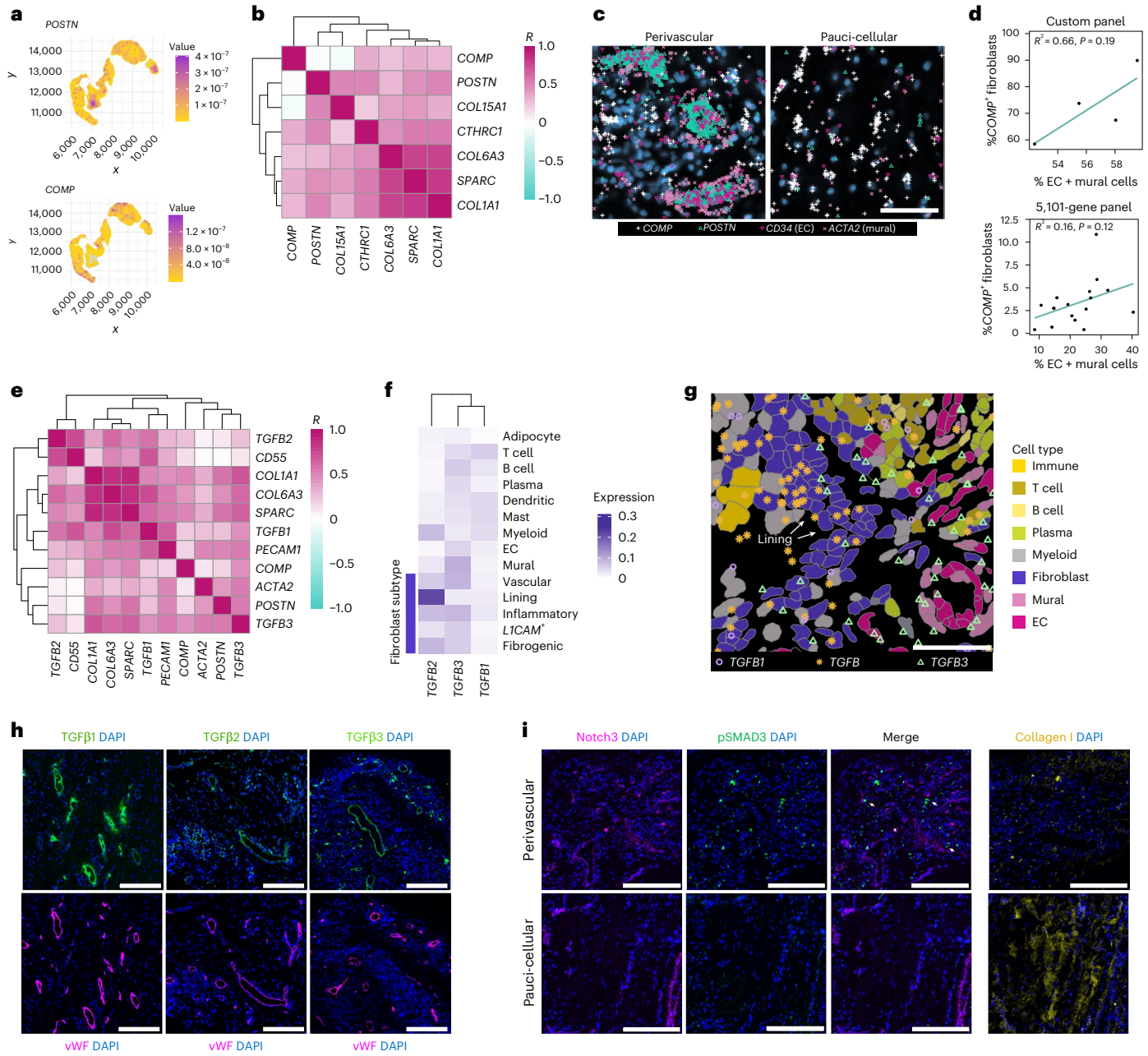

Fig. 3 | Perivascular compartmentalization of TGFβ signaling. a, Visualization of kernel density estimates of *POSTN* (top) and *COMP* (bottom) expression within a representative *COL1A1*-high region. **b**, Heat map showing mean pixel correlations across synovial samples ($n = 4$) between kernel densities for selected fibrogenic genes within *COL1A1*-high regions. **c**, Representative examples ($n = 4$ RA tissues) of *COMP* transcript expression in perivascular and pauci-cellular regions. Scale bar, 50 µm. **d**, Correlation between the percentage of fibroblasts that express *COMP* (count > 0) per sample and abundance of endothelial and mural cells as a percentage of total cells in the same sample. Statistics calculated by two-sided Pearson's correlation coefficient test. Top: 4 samples analyzed with a 50-gene custom panel. Bottom: 16 samples analyzed with a 5,101-gene panel. **e**, Mean pixel correlations across samples ($n = 4$) for *TGFB* isoform expression compared to selected fibroblast and endothelial markers. **f**, Heat map representing relative expression of *TGFB* isoforms across different cell types in synovial samples ($n = 17$) analyzed with a 5,101-gene panel. **g**, Example of data in **f** showing *TGFB* transcripts overlaid on cell types. Scale bar, 50 µm. **h**, Immunofluorescence staining of RA synovial tissue showing protein expression of TGFβ isoforms relative to EC marker vWF. TGFβ3 and vWF staining were performed on serial sections. **i**, Immunofluorescence data showing Notch3, Collagen 1 and pSMAD3 staining in perivascular and pauci-cellular regions of the RA synovium. Scale bars, 200 µm. Immunofluorescence is representative of $n > 5$ RA synovial tissue.

in the PEAC bulk RNA-seq data, in contrast to *COMP*-coexpressed genes, which were more associated with treatment nonresponse (Extended Data Fig. 4c,d). Accordingly, the *COMP*^{hi} fibroblast cluster exhibited striking enrichment of the nonresponder signature compared to the *POSTN*^{hi} and *CXCL12*^{hi} fibrogenic subclusters, suggesting that *COMP* expression, specifically denotes the subset of fibrogenic fibroblasts in RA associated with treatment resistance[33,34] (Fig. 2e). At the transcript level, *COMP* was more elevated in the treatment-naive biopsy samples of patients who failed to achieve remission compared to *DKK3*, *FMOD* or *POSTN* (Fig. 2e and Extended Data Fig. 4e) and was more broadly enriched across non-remission niches (Extended Data Fig. 4f). Additionally, baseline *COMP*$^{+}$ cell abundance correlated with reduced 6-month and 12-month improvements in tender joint counts (delTJC28) in the non-remission group (Extended Data Fig. 4g). Further,

https://doi.org/10.1038/s41590-025-02386-2

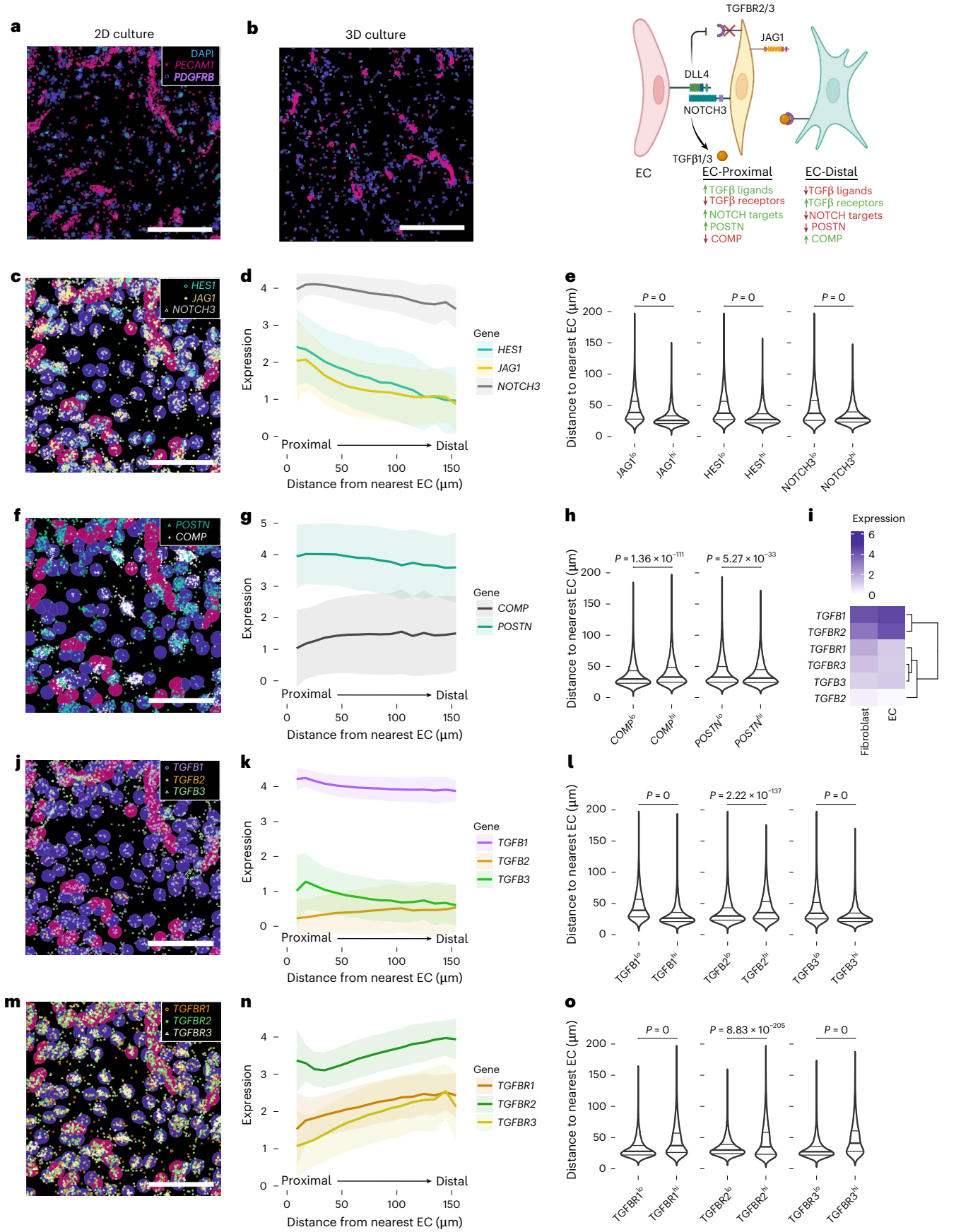

there was a positive trend among the remission and non-remission groups between baseline *COMP*$^+$ cell abundance and DAS28-ESR at 12 months, highlighting the link between *COMP*$^+$ cell abundance and longer-term disease activity (Extended Data Fig. 4g).

Next, to investigate tissue niches in which increased fibrogenic activation might drive differences in remission status, we first classified all niche tiles into low, medium and high for fibrogenic signature expression (Fig. 2f and Extended Data Fig. 4h). Immune and lining

Fig. 4 | ECs generate a proximal-to-distal gene expression pattern in surrounding fibroblasts. a,**b**, Representative visualization of spatially profiled 2D (**a**) and 3D (**b**) co-culture with transcripts for fibroblast marker *PDGFRB*, and endothelial marker *PECAM1*, overlaid on DAPI. Schematic summarizing the spatial distribution of fibroblast transcripts based on EC proximity on the right. **c**,**f**,**j**,**m**, Example images of gene expression distribution overlaid on labeled cell types, to a maximum of randomly selected 1,500 transcripts per gene, with Notch target genes shown in **c**, fibrogenic markers in **f**, *TGFB* ligands in **j** and *TGFB* receptors in **m**. **d**,**g**,**k**,**n**, Line plots representing average expression of transcripts per fibroblast relative to the EC distance, with Notch target genes shown in **d**, fibrogenic markers in **g**, *TGFB* ligands in **k** and *TGFB* receptors in **n**. Solid line shows the mean; shaded regions show one standard deviation. **e**,**h**,**l**,**o**, Distance to the nearest EC in the top-versus-bottom quantile of cells by expression of each gene, with Notch target genes shown in **e**, fibrogenic markers in **h**, *TGFB* ligands in **l** and *TGFB* receptors in **o**. Statistics by two-sided Wilcoxon tests comparing distances from ECs for the top-versus-bottom quantiles of cells in expression of each gene. **i**, Heat map representing expression of *TGFB* ligands and receptors by cell type in the co-culture. Scale bars, 200 µm (**a**–**c**, **f**, **j** and **m**). Schematic in **b** created with BioRender.com.

niches were highly represented among tiles with low and medium fibrogenic expression, whereas fibroblast-rich, stromal-adipose and vascular tiles were prominently represented among tiles with high fibrogenic signatures, consistent with nonresponder signature enrichment. Among the three relevant niches, fibrogenic scores in only the vascular niche were elevated in non-remission, suggesting that vascular-associated fibrogenic activity may drive treatment nonresponse (Fig. 2g and Extended Data Fig. 4i).

Perivascular compartmentalization of TGFβ signaling

To improve localization of fibrogenic fibroblasts in synovial tissue, we designed a targeted panel of 50 stromal-associated genes for spatial transcriptomics analysis of additional RA synovial tissue samples ($n = 4$). The smaller panel enhanced the detection of relevant transcripts, including TGFβ isoforms, key regulators of fibrosis[19] and *COMP* (~14-fold increased detection). Gating on fibrogenic tissue regions, defined by high *COL1A1* expression, we found that *COMP* and *POSTN* transcript kernel density estimates mapped to spatially distinct areas (Fig. 3a,b), consistent with their differential single-cell expression patterns[15]. We observed two major patterns of *COMP*^{hi} fibroblast localization: (1) within pauci-cellular fibroblast-rich regions and (2) within the distal layers of perivascular regions, surrounding mural cells and vascular fibroblasts (Fig. 3c). Accordingly, patient-level analysis of the spatial data revealed a positive association between the proportion of vascular cells and the abundance of *COMP*-expressing fibroblasts (Fig. 3d). *POSTN* transcripts, in contrast, were coexpressed with mural cell (*ACTA2*) and vascular fibroblast (*COL15A1*) markers, indicating strong expression of *POSTN* in the proximal cell layers of vascular regions (Fig. 3e and Supplementary Fig. 1a). Together, our data indicate that both subsets of fibrogenic fibroblasts localize to the perivascular compartment in RA synovia, but in distinct layers.

We next asked whether TGFβ isoform expression is spatially associated with fibrogenic niches in RA (Fig. 3e). *TGFB1* colocalized with the lining fibroblast marker *CD55* and endothelial cell (EC) marker *PECAM1*. *TGFB2* transcripts strongly colocalized with *CD55*. *TGFB3* transcripts not only colocalized with markers of endothelial (*PECAM1*) and mural (*ACTA2*) cells, suggesting vascular and perivascular enrichment, but also overlapped with fibrogenic transcripts, including *POSTN*, *COMP* and *COL1A1*, indicating broad coexpression within fibrogenic populations. Analysis of TGFβ isoform expression by cell type in 396.10 spatial transcriptomic data confirmed lining fibroblast-specific expression of *TGFB2*, diffuse expression of *TGFB1* and stromal-vascular-enriched *TGFB3* expression (Fig. 3f,g and Supplementary Fig. 1b).

Immunofluorescence staining of synovial tissue revealed perivascular localization of TGFβ1, TGFβ2 and TGFβ3 protein (Fig. 3h), although TGFβ2 also appeared in immune aggregates. Accordingly, we observed that a specific indicator of active TGFβ signaling, pSMAD3, was restricted to fibroblasts in vascular regions and absent in pauci-cellular regions characterized by dense collagen deposition (Fig. 3i and Supplementary Fig. 1c), suggesting that active TGFβ signaling occurs specifically in the vascular compartment. Together, the observed spatial patterning of both fibrogenic gene expression and TGFβ indicates that the perivascular niche is an important hub for fibrogenic signaling.

ECs spatially pattern TGFβ responsiveness

To better understand how vascular ECs generate spatial patterning of TGFβ signaling in fibroblasts, we modeled and spatially profiled co-cultures of human umbilical vein endothelial cells (HUVECs) with synovial fibroblasts in two-dimensional (2D) and in three-dimensional (3D) systems (Fig. 4a,b). In both systems, we observed distinct fibroblast transcriptional programs as a function of proximity to the nearest EC: fibroblasts in the most proximal layer expressed Notch target genes including *JAG1*, *HES1* and *NOTCH3*, which decreased in distal layers of fibroblasts that were over one cell layer away (Fig. 4c–e and Extended Data Fig. 5a–c). Like Notch target genes, *POSTN* expression was also highest on the proximal layer of fibroblasts adjacent to ECs and gradually decreased in distal fibroblasts, in contrast to *COMP* expression, which increased in distal compartments (Fig. 4f–h and Extended Data Fig. 5d–f). Collectively, EC-derived signals pattern fibrogenic gene expression in a proximal-to-distal manner, where *POSTN* represents an EC-proximal program and *COMP* expression represents an EC-distal program.

Next, we evaluated the distribution of TGFβ isoforms and their receptors along the EC proximal-to-distal axis to identify receptor–ligand pairs responsible for differential fibroblast responses to TGFβ. Consistent with the expression pattern in RA synovia, *TGFB1* was expressed on ECs and on the EC-proximal fibroblast layer, with fewer average transcripts in EC-distal fibroblasts (Fig. 4i–l and Extended Data Fig. 5h–j), while *TGFB2* was lowly and diffusely expressed. *TGFB3*, like *TGFB1*, was induced on endothelial-proximal fibroblasts and then sharply decreased in EC-distal fibroblasts. Transcripts of *TGFBR1*, the TGFβ signaling co-receptor, *TGFBR2*, the ligand-binding receptor, and *TGFBR3*, a high-affinity TGFβ binding co-receptor for all isoforms[35,36], were lowest in EC-proximal

Fig. 5 | Notch signaling controls TGFβ isoform and receptor expression in synovial fibroblasts. a, UMAP plot of isolated single cells from the indicated 3D co-culture conditions[9]. Fibroblast monoculture: organoid containing fibroblasts only; Fibroblasts + ECs: organoids containing fibroblasts and ECs; Fibroblasts + ECs + DAPT: organoids containing fibroblasts and ECs treated with a Notch inhibitor. **b**, UMAP plot of cells from organoid culture shaded by level of fibrogenic gene signature score calculated with UCell. **c**, Dot plots representing the expression of selected genes by condition. The asterisk indicates genes and conditions with $P < 1 \times 10^{-100}$ between monoculture and co-culture. **d**,**e**, RT–qPCR analysis of *TGFB* isoform (**d**) and receptor gene expression (**e**) on unstimulated or DLL4-stimulated fibroblasts treated with or without DAPT (10 µM) for 72 h. **f**,**g**, Immunoblots of TGFβ isoforms (**f**) and receptors (**g**) with lysates from unstimulated or DLL4-stimulated fibroblasts (72 h). Data are representative of three independent experiments. **h**, RT–qPCR analysis of *COL1A1*, *COL3A1* and *COL6A1* gene expression on unstimulated or DLL4-stimulated fibroblasts treated with or without TGFβ inhibitor (SB431542; 10 µM) or DAPT (10 µM) for 72 h. **i**, ELISA quantification of fibroblast production of pro-collagen I alpha 1 in 3 cell lines over 24 h after 3 days of treatment with siRNA (20 nM) with or without DLL4 stimulation. **j**,**k**, ELISA quantification of fibroblast production of POSTN (**j**) and COMP (**k**) over 24 h after 3 days of treatment with siRNA (20 nM) with or without DLL4 stimulation. For **d**, **e** and **h**, each data point represents an independent cell line ($n = 6$); for **i**–**k**, each data point represents biological replicates ($n = 3$) from a single-cell line and are representative of at least two independent experiments. Data are shown as the mean ± s.d. Statistical analysis was performed by a two-sided ratio paired *t*-test for **d**, **e** and **h**, two-sided Bonferroni-corrected Wilcoxon test for **c** and unpaired two-sided *t*-tests for **i**–**k**.

https://doi.org/10.1038/s41590-025-02386-2

layers and gradually increased in EC-distal fibroblasts (Fig. 4m–o and Extended Data Fig. 5k–m); the observations were concordant across both the 2D and 3D culture systems. Collectively, these data suggest that endothelial-derived signals determine spatial patterning of TGFβ signaling via paired regulation of TGFβ ligands and receptors.

Patterning of TGFβ responsiveness via Notch signaling

Given the distinct spatial pattern of TGFβ-related transcripts in fibroblasts generated by contact with neighboring ECs, we evaluated the potential role of endothelial-derived Notch in regulating TGFβ signaling. We reanalyzed scRNA-seq data from Matrigel-embedded

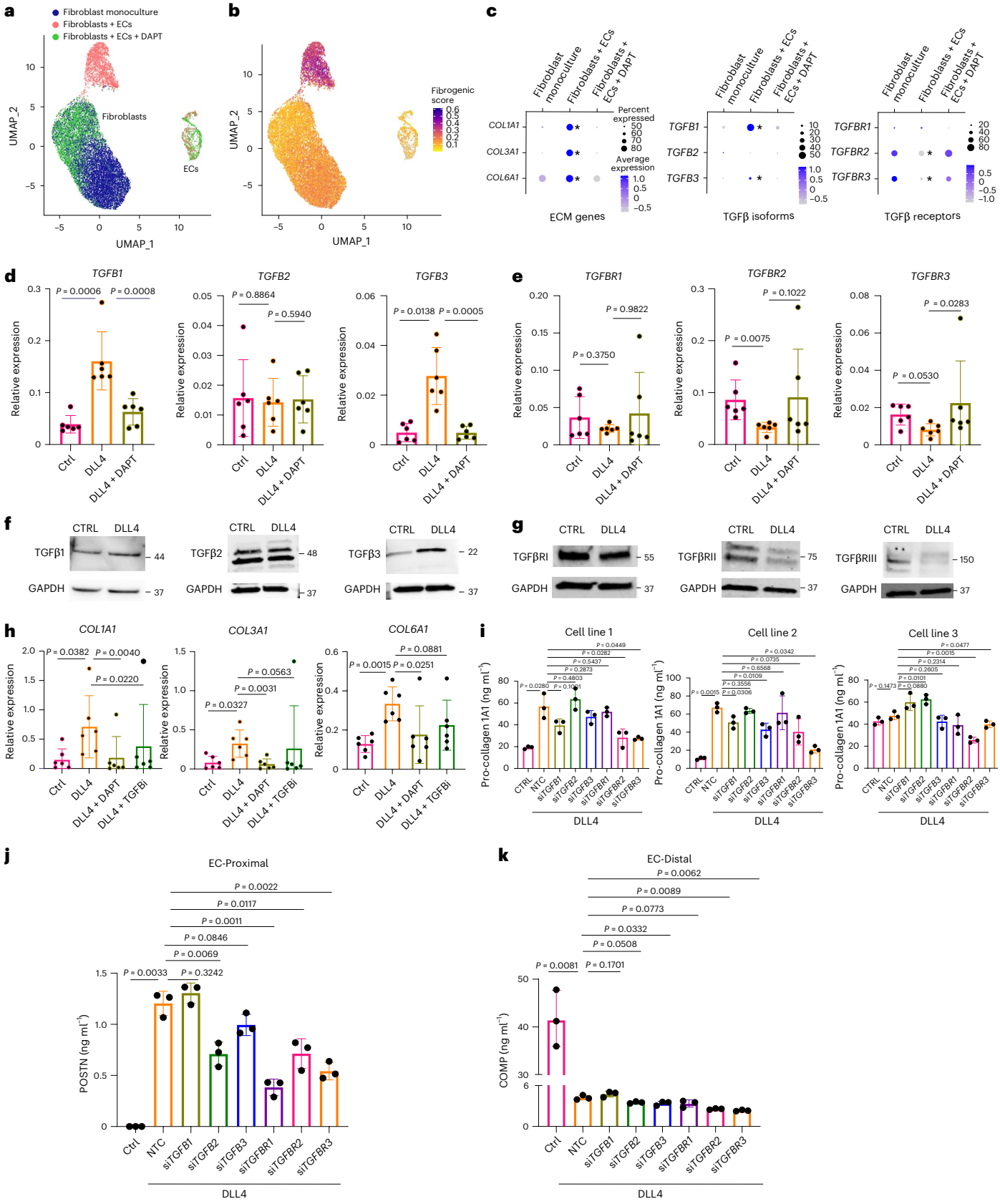

https://doi.org/10.1038/s41590-025-02386-2

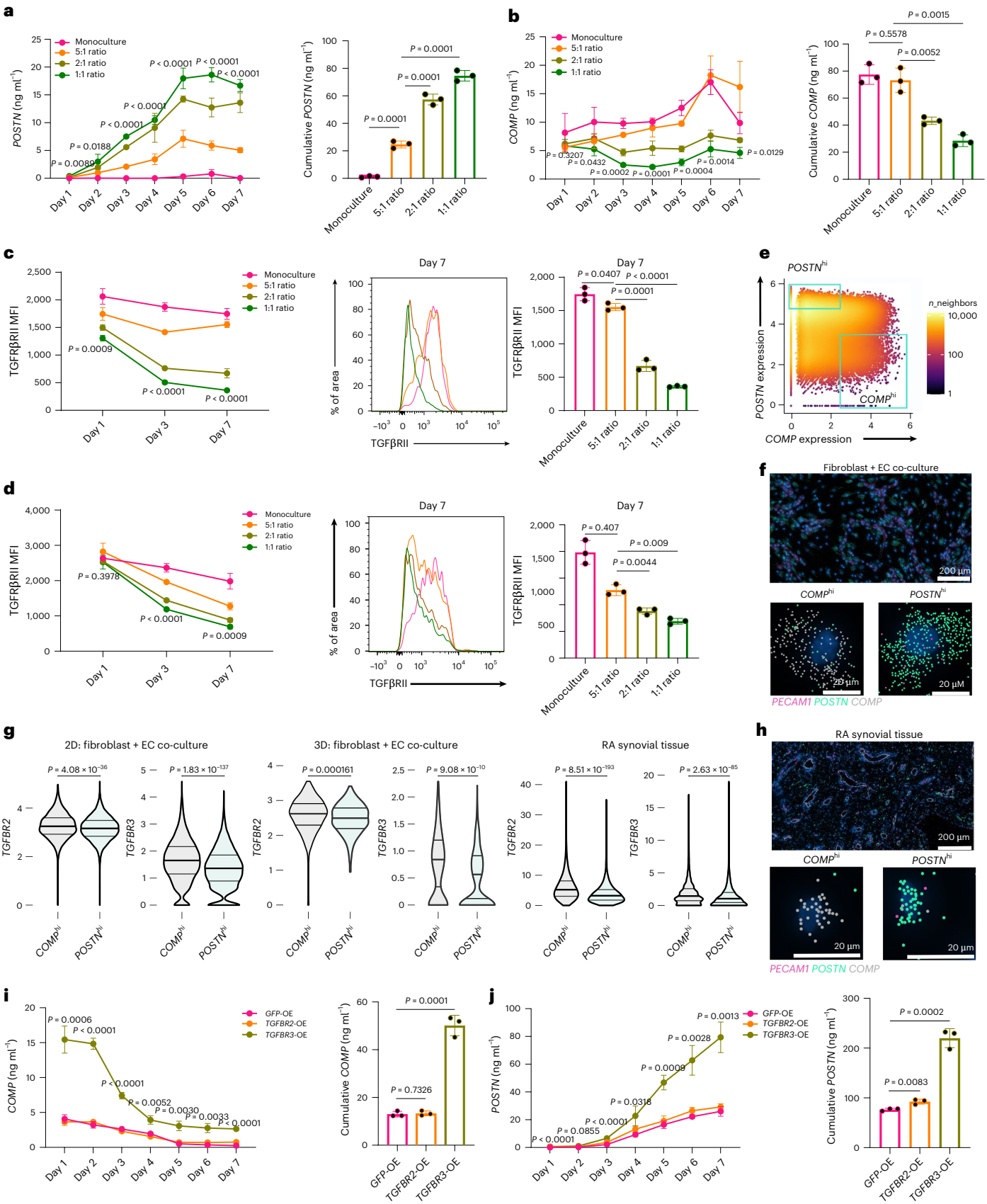

3D organoids of fibroblasts and ECs treated with or without the Notch inhibitor DAPT[9] (Fig. 5a–c and Extended Data Fig. 6a). We observed significant induction of *TGFB1*, *TGFB3* and fibrogenic gene expression when ECs were included in organoids as well as suppression of *TGFBR2* and *TGFBR3* expression (Fig. 5c). The addition of DAPT reversed *TGFB* induction and *TGFBR* suppression, directly implicating Notch signaling as an upstream regulator of fibroblast TGFβ signaling.

Fig. 6 | Endothelial-derived Notch signaling dictates fibroblast TGFβ responsiveness via regulation of TGFβ receptor III. a–**d**, A fixed number of fibroblasts were seeded with varying numbers of HUVECs. Monoculture: 5,000 fibroblasts, 5:1 ratio: 5,000 fibroblasts and 1,000 HUVECs, 2:1 ratio: 5,000 fibroblasts and 2,500 HUVECs, 1:1 ratio: 5,000 fibroblasts and 5,000 HUVECs. **a**,**b**, ELISA quantification of POSTN (**a**) and COMP (**b**) production during co-culture. *P* values in the line graphs are displayed for the comparisons between monoculture and 1:1 ratio. The respective bar charts to the right represent the area under the curve. **c**,**d**, Flow cytometric quantification of fibroblast TGFβRII (**c**) and TGFβRIII (**d**) at the indicated days during co-culture with ECs. *P* values are shown for comparisons between monoculture and 1:1 ratio. Representative flow cytometry histograms and mean fluorescence intensity (MFI) quantification for day 7 of co-culture are shown. **e**, Gating strategy for classifying *COMP*^{hi} and *POSTN*^{hi} fibroblasts from the Xenium-profiled co-culture (mutually exclusive top quantile of cells expressing each gene, with *POSTN* ≤ 3.5 for *COMP*^{hi}). **f**, Representative examples of *COMP*^{hi} and *POSTN*^{hi} fibroblasts in 2D culture are shown with transcripts. **g**, Violin plot showing the distribution of *TGFBR2* and *TGFBR3* transcripts on *POSTN*^{hi} and *COMP*^{hi} gated fibroblasts in 2D co-culture, 3D co-culture and RA synovium. **h**, Representative example ($n = 4$ RA synovial tissue) of gated (mutually exclusive top quantiles of expressing cells) *COMP*^{hi} and *POSTN*^{hi} synovial fibroblasts with transcripts. **i**,**j**, ELISA quantification of COMP (**i**) and POSTN (**j**) production from co-culture of fibroblasts overexpressing (OE) *GFP*, *TGFBR2* or *TGFBR3* with ECs in a 1:1 ratio. *P* values are shown for the comparison between *TGFBR3*-OE and *GFP*-OE data points. The bar plot on the right represents the area under the curve. Data points are shown as the mean ± s.d., represent $n = 3$ biological replicates and are representative of at least two independent experiments. For statistical analysis, a two-tailed Student's *t*-test was used for **a**–**d**, **i** and **j**, and a two-sided Wilcoxon test was used for **g**.

A 2D culture system showed similar effects of Notch activation on fibroblast TGFβ signaling. We stimulated synovial fibroblast cell lines ($n = 6$) with plate-bound DLL4 and observed strong induction of *TGFB1* and *TGFB3* gene and protein expression and suppression of *TGFBR2* and *TGFBR3* that was reversed with the addition of DAPT (Fig. 5d–g). Further, there were significant peaks in the promoter regions of *TGFBR2* and *TGFBR3* for binding of a Notch-associated transcription factor (RBPJ) in HepG2 cells, supporting a role for Notch in direct transcriptional regulation of TGFβ receptors (Extended Data Fig. 6b).

Next, we assessed the impact of Notch and TGFβ signaling on fibrogenic gene expression and observed induction of fibrogenic collagens (*COL1A1*, *COL3A1*, *COL6A1*) with DLL4 stimulation that was reversed with the addition of DAPT or TGFβ inhibitor (SB431542; Fig. 5h). We evaluated the extent to which Notch-mediated TGFβ signaling occurs in a cell contact-dependent or soluble manner (Extended Data Fig. 6c–f). Low concentrations of soluble TGFβ1 were induced in the supernatant of DLL4-stimulated cells (Extended Data Fig. 6c), but conditioned medium from DLL4-stimulated fibroblasts was unable to induce TGFβ-responsive genes in recipient fibroblasts (Extended Data Fig. 6d). Similarly, when we cultured fibroblasts in a Transwell chamber above DLL4-stimulated fibroblasts, we observed no induction of TGFβ signaling (Extended Data Fig. 6e). Additionally, antibody blockade against individual or pan-TGFβ isoforms did not substantially diminish ECM production. Altogether, our findings suggest that Notch-induced TGFβ signaling primarily occurs in a contact-dependent manner (Extended Data Fig. 6f).

We then systematically tested the effects of each TGFβ isoform and receptor for Notch-mediated fibrogenic signaling (Fig. 5i–k and Extended Data Fig. 6g–i). siRNA knockdown of *TGFB* diminished pro-collagen 1 alpha 1 (PRO-COL1) production in two of three cell lines for si*TGFB1*, one of three cell lines for si*TGFB2* and one of three cell lines for si*TGFB3*. Combinatorial knockdown of pairs of TGFβ isoforms (Extended Data Fig. 6h) did not significantly diminish PRO-COL1, suggesting redundant roles for all three TGFβ isoforms in mediating Notch-driven fibrogenic signaling in vitro. Among TGFβ receptors, knockdown of *TGFBR1* did not significantly alter pro-collagen production (Extended Data Fig. 6g), whereas *TGFBR2* knockdown diminished production in two of three cell lines and *TGFBR3* knockdown diminished production in three of three cell lines (Fig. 5i). Combinatorial knockdown of *TGFBR2* and *TGFBR3* diminished PRO-COL1 production the most, suggesting that expression levels of these receptors more strongly regulate PRO-COL1 compared to *TGFBR1* (Extended Data Fig. 6h). Subsequently, we examined how DLL4 stimulation regulated the distinct EC-proximal (*POSTN*) and EC-distal (*COMP*) fibrogenic programs (Fig. 5j,k and Extended Data Fig. 6i). Although the production of both proteins was strongly induced by soluble TGFβ (Extended Data Fig. 6f), POSTN was potentiated by Notch signaling, whereas COMP was highly suppressed, and both were diminished with *TGFBR2* and *TGFBR3* knockdown. Overall, while the responses of *COMP* and *POSTN* expression to soluble TGFβ and TGFβ receptor knockdown were similar, opposing impacts of Notch signaling on *COMP* and *POSTN* implicated an additional mechanism by which Notch regulates the patterning of TGFβ responsiveness in fibroblasts.

To quantify the temporal dynamics of EC-derived Notch in regulating fibrogenic programs, we first set up 2D and 3D co-cultures treated with or without DAPT and TGFβi, collecting and replacing media every 24 h to measure interval production of POSTN, COMP and PRO-COL1 (Extended Data Fig. 7a,b). In both systems, co-cultured fibroblasts exhibited sustained production of PRO-COL1 and POSTN compared to monocultured fibroblasts and was diminished with DAPT or TGFβi. In contrast, COMP production temporally decreased in co-culture, consistent with the suppression of *COMP* expression by endothelial-derived Notch signaling. Next, we cultured a fixed number of fibroblasts with varying numbers of ECs, measuring interval protein production. In an EC ratio-dependent manner, POSTN production was significantly induced, whereas COMP production was suppressed (Fig. 6a,b). Furthermore, the suppression of COMP production mirrored the temporal EC ratio-dependent downregulation of TGFβRII and TGFβRIII, suggesting that changes in fibroblast TGFβ receptor availability may create a dynamic threshold on the ability of fibroblasts to respond to TGFβ (Fig. 6c,d). Accordingly, analysis of Xenium co-culture and synovial tissue data revealed significantly higher expression of *TGFBR2* and *TGFBR3* in *COMP*^{hi} fibroblasts compared to *POSTN*^{hi} fibroblasts (Fig. 6e–h).

Fig. 7 | Disruption of steady-state Notch patterning activates a *COMP*^{hi} fibrogenic program. a,**b**, ELISA quantification of POSTN (**a**) and COMP (**b**) production from fibroblasts and EC co-culture (1:1 ratio) treated with the indicated siRNAs (20 nM). *P* values are shown for the comparison between DLL4 siRNA and control siRNA conditions (cumulative POSTN $P < 0.0001$, cumulative COMP $P = 0.0081$). The bar plots to the right represent the area under the curve. **c**–**n**, RNAscope quantification of fibrogenic program in response to Notch perturbation. Representative images of siControl-treated and siRNA against *DLL4* (siDLL4)-treated co-cultures with indicated fibrogenic (**a**–**f**), *TGFB* (**g**–**j**) and *TGFBR* (**k**–**n**) transcripts shown. PECAM and DLL4 transcripts denote endothelial cells. Scale bars, 200 µm. **d**,**f**,**h**,**j**,**l**,**n**, Boxen plots representing the distribution of MFIs of the corresponding genes in siControl and siDLL4 conditions on the indicated number of cells selected for quantification. **d**,**f**,**l**,**n**, Ribbon plots showing spatial gene expression patterns in relation to EC proximity for indicated genes between siRNA conditions. Solid line shows the mean intensity, and shaded regions show one standard deviation. **d**,**f**, Violin plots showing the distance to the nearest EC (in µm) for *POSTN*^{hi} and *COMP*^{hi} cells, defined as cells with the highest quantile of *POSTN* and *COMP* fluorescence intensity, respectively. *P* values for the comparisons between siCtrl and siDLL4 are $P < 6 \times 10^{-51}$ and $P < 2 \times 10^{-308}$ for *TGFB3* (**j**) and *TGFBR3* (**n**), respectively. The data in **a** and **b** are shown as means ± s.d., represent $n = 3$ biological replicates and are representative of at least two independent experiments. A two-tailed unpaired Student's *t*-test was performed for **a** and **b** and two-tailed Wilcoxon tests for **d**, **f**, **h**, **g**, **l** and **n**. In the boxen plots, boxes show nested quantile ranges (median, 25–75%, 12.5–87.5%, 6.25–93.75%, and so on), the center line shows the median (50th percentile), the whiskers represent minimum and maximum values, and the outliers are shown as individual points outside the whiskers.

https://doi.org/10.1038/s41590-025-02386-2

Next, to determine the extent to which suppression of COMP production in co-culture was mediated by dynamic TGFβ receptor downregulation, we used lentivirus to overexpress TGFBR2 and TGFBR3 in fibroblasts (Fig. 6i,j and Extended Data Fig. 7c). ECs co-cultured with fibroblasts overexpressing *TGFBR3*, but not *TGFBR2*, had significantly diminished suppression of COMP. Moreover, daily POSTN production was significantly enhanced in co-cultures with *TGFBR3*-overexpressing fibroblasts, despite negligible effects of *TGFBR2* and *TGFBR3* on the fibroblast response to TGFβ itself, suggesting that modulation of TGFβRIII availability is specific to endothelial-derived Notch signaling in patterning of TGFβ responsiveness (Extended Data Fig. 7d,e).

Notch disruption induces fibrogenic activation

Since we established that steady-state EC-derived Notch signaling generates a proximal-to-distal axis of TGFβ response in fibroblasts, we next sought to understand the consequences of disrupting steady-state patterning on fibrogenic gene expression. We hypothesized that disruption of a steady-state Notch signaling can activate expression of

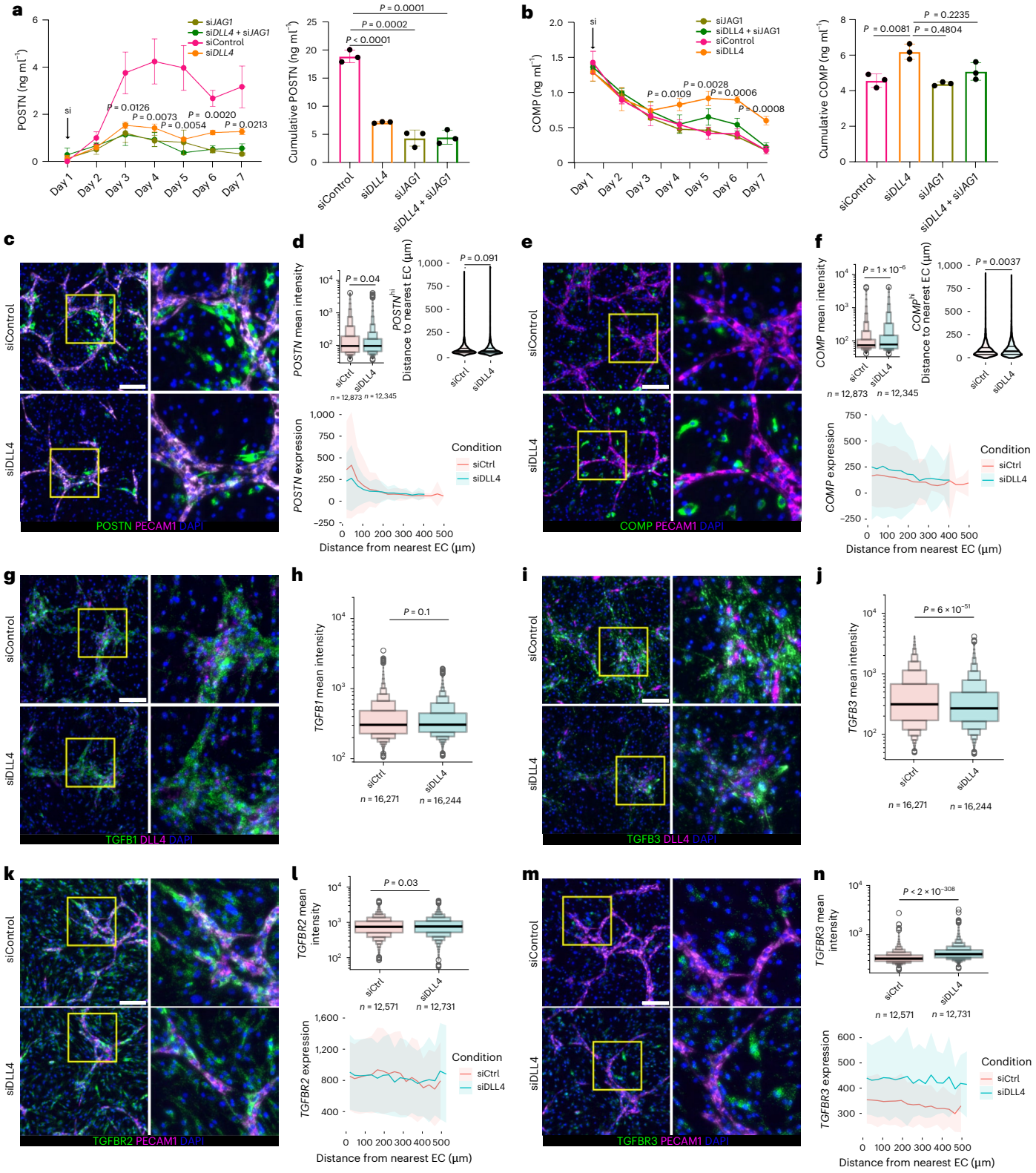

EC-distal gene expression programs. Knockdown of EC-specific Notch ligand DLL4, fibroblast-expressed JAG1 or a combination of both at the start of co-culture significantly diminished POSTN (Fig. 7a,b). COMP was suppressed through day 3 but was de-repressed starting on day 4 in the DLL4 knockdown condition (Fig. 7b).

To characterize alterations in spatial patterning resulting from disruption of steady-state Notch signaling, we applied in situ hybridization to co-cultures treated with control or DLL4 siRNA (Supplementary Fig. 1a). As at the protein level, we observed significant induction of *COMP* expression ($P = 1.4 \times 10^{-6}$) and diminishment of *POSTN* expression ($P = 0.04$) in the *DLL4* knockdown condition (Fig. 7c–f). When we compared the average expression of *POSTN* in relation to EC distance, we observed no significant changes, as expected, given its EC-proximal restricted patterning (Fig. 7c,d). In contrast, we observed that average *COMP* expression was higher with *DLL4* knockdown compared to control and that the average distance of *COMP*^{hi} cells to ECs increased (Fig. 7e,f). We also examined the effect of *DLL4* knockdown on TGFβ isoform and receptor expression (Fig. 7g–n). While we observed no significant changes in the patterns of *TGFB1* and only modest changes for *TGFBR2* expression across cells (Fig. 7g,h,k,l), we observed a significant increase in the average expression of *TGFBR3* and decrease in the average expression of *TGFB3* (Fig. 7i,j,m,n). As with *COMP* expression, we observed elevated *TGFBR3* expression in both EC-proximal and EC-distal compartments of *DLL4* knockdown co-culture (Fig. 7n). Together, these data suggest that the expansion of *COMP*-expressing fibroblasts was specifically linked to the de-repression of TGFβRIII mediated by *DLL4* knockdown, rather than increases in TGFβ expression, a potential mechanism by which EC-derived Notch signaling dictates the spatial patterning of fibrogenic signaling.

To examine the extent to which *COMP* expression is linked to Notch-mediated tuning of fibroblast sensitivity in synovial tissue, we scored vascular niches according to their expression of Notch transcriptional targets (Supplementary Fig. 2b). *TGFBR3* expression was negatively correlated with vascular Notch activation scores across biopsy samples, supporting the role of Notch signaling in suppressing TGFβ receptor expression in vivo. Collectively, our in vitro and in vivo results suggest that Notch can tune TGFβ sensitivity via TGFβ receptor regulation in vascular niches.

Posttreatment expansion of fibrogenic niches

Next, we evaluated the effect of treatment on fibrogenic signaling by analyzing 17 paired posttreatment synovial biopsy samples (Fig. 8a–c and Extended Data Fig. 8a–f). Across patients we observed substantial depletion of immune niches and immune subtypes and relative expansion of fibroblast-rich niches regardless of response status or treatment arm (Fig. 8b). Accordingly, tissue niche composition and swollen joint counts (SJC44, $P = 0.2273$) did not significantly differ between patients who achieved remission and those who did not (Extended Data Fig. 8f,g and Supplementary Table 1). However, while DAS28-ESR components decreased across remission groups, non-remission status was driven by significantly higher tender joint counts (TJC53, $P = 0.0037$) and VAS pain scores ($P = 0.0233$; Supplementary Table 1 and Extended Data Fig. 8g).

Examination of fibrogenic gene expression in fibroblasts from posttreatment biopsy samples revealed elevation of the fibrogenic signature across groups (Fig. 8c and Extended Data Fig. 8h). Accordingly, we observed increases in the percentage of fibroblasts expressing *COMP* in most patients (remission/borderline, 5/10 patients; non-remission, 6/7 patients), with starker increases under DMARD treatment (Fig. 8d and Extended Data Fig. 8i). *COMP*^{hi} tissue regions became more pauci-cellular after treatment, with an inverse relationship between *COMP*$^{+}$ cell abundance and *COMP*$^{+}$ cell density (Fig. 8d–f). These data suggest that after treatment, *COMP*-expressing fibroblasts expand and may deposit fibrous ECM. Over time, this process could generate pauci-cellular niches, thus supporting active fibrogenic remodeling in the fibroblast-rich compartment of RA following immune depletion.

Next, we evaluated whether serum markers could be used as surrogates to track fibrogenic activity in synovium by profiling pretreatment and posttreatment serum with an ~5,400-plex protein panel (Olink; Extended Data Fig. 9a,b). Neither individual fibrogenic proteins nor inflammatory markers showed significant trends by time point or remission group (Extended Data Fig. 9a). A number of stromal markers, including EGFL7 ($r = 0.685$), an endothelial-expressed angiogenic factor[37], were highly correlated with the fibrogenic score or change in fibrogenic score, although they did not meet significance (Extended Data Fig. 9b). Therefore, we extended our analysis to the AMP cohort[15] to identify which cell-type abundance (CTAP) phenotype was most associated with fibrogenic signaling (Extended Data Fig. 9c–f). Fibroblasts from the CTAP characterized by endothelial, fibroblast and myeloid cells (CTAP-EFM) were the most strongly enriched for the fibrogenic gene signature and *COMP* expression compared to fibroblasts from other CTAPs (Extended Data Fig. 9c). Interestingly, patients belonging to CTAP-EFM, on average, also had significantly longer disease duration (Extended Data Fig. 9d). We performed differential abundance analysis of serum proteins in CTAP-EFM patients ($n = 7$) versus those classified as belonging to other CTAPs ($n = 60$). In patients belonging to CTAP-EFM, we observed enrichment of several established fibrogenic markers including SPARC, OGN and CCN2 (Extended Data Fig. 9e,f). Collectively, these data support fibrogenic remodeling in a subset of patients with RA who have a longer disease duration and the potential to capture proteomic signatures at later stages of disease when joint activity may be reflected systemically[38].

Finally, we evaluated the feasibility of targeting Notch and TGFβ signaling to diminish fibrogenesis in RA synovial tissue (Fig. 8g–j and Extended Data Fig. 10a–e). We obtained synovial tissue from patients with active RA ($n = 6$), generated >30 patient-derived organoids (PDOs) from each tissue with a 2-mm punch biopsy tool, and treated each PDO with dimethylsulfoxide (DMSO), DAPT or TGFβi for 72 h after overnight rest, collecting media after the initial overnight incubation to establish the baseline per-PDO fibrogenic protein secretion. Across RA donors, we observed relatively high and variable production of COMP, POSTN and PRO-COL1 (Fig. 8h). Treatment of RA PDOs with both DAPT and TGFβi resulted in a significant reduction of COMP, POSTN and PRO-COL1 (Fig. 8h and Extended Data Fig. 10a). We applied the

Fig. 8 | Active fibrogenic signaling can be abrogated with Notch and TGFβ inhibition. a, UMAPs showing labeled posttreatment niche tiles. **b**, Quantification of the relative abundance of immune and fibroblast-rich niches before treatment and after treatment ($n = 16$ patients). Line colors indicate remission status. **c**, Density plot of fibrogenic UCell scores by time and remission status. Color gradient represents the density of cells expressing the indicated score, with dashed lines indicating percentile score distributions per biopsy category. **d**, Quantification of *COMP*$^{+}$ fibroblast abundance and cell density before treatment and after treatment ($n = 11$ DMARD-treated, $n = 6$ adalimumab-treated). **e**, Correlation between changes in the percentage of fibroblasts that express *COMP* and the cell density of *COMP*^{hi} regions per patient after 6 months of treatment. Statistics by two-sided Pearson correlation test. **f**, Representative *COMP* gene expression and paired H&E for a pretreatment and posttreatment biopsy from a borderline patient. *VWF* marks vasculature. Scale bar, 50 µm. **g**, Schematic summarizing the PDO experiments and representative transcript density plots for spatially profiled PDOs showing genes that highlight core synovial tissue structures. Scale bar, 1 µm. **h**, ELISA data showing supernatant levels of POSTN, COMP and PRO-COL1 in PDOs incubated overnight (left), alongside the median per-patient $\log_2$ fold change of these proteins after 3 days of treatment, normalized to overnight per-organoid protein production ($n = 10$–13 PDOs per condition). Statistics by Gaussian GLM, patient included as a cofactor, with FDR correction. **i**,**j**, Representative images of transcript expression in indicated conditions (top) and per-PDO average mural cell (**i**) and fibroblast (**j**) expression of indicated genes (bottom). In **b**, **d**, **i** and **j**, a two-sided Wilcoxon test was used.

https://doi.org/10.1038/s41590-025-02386-2

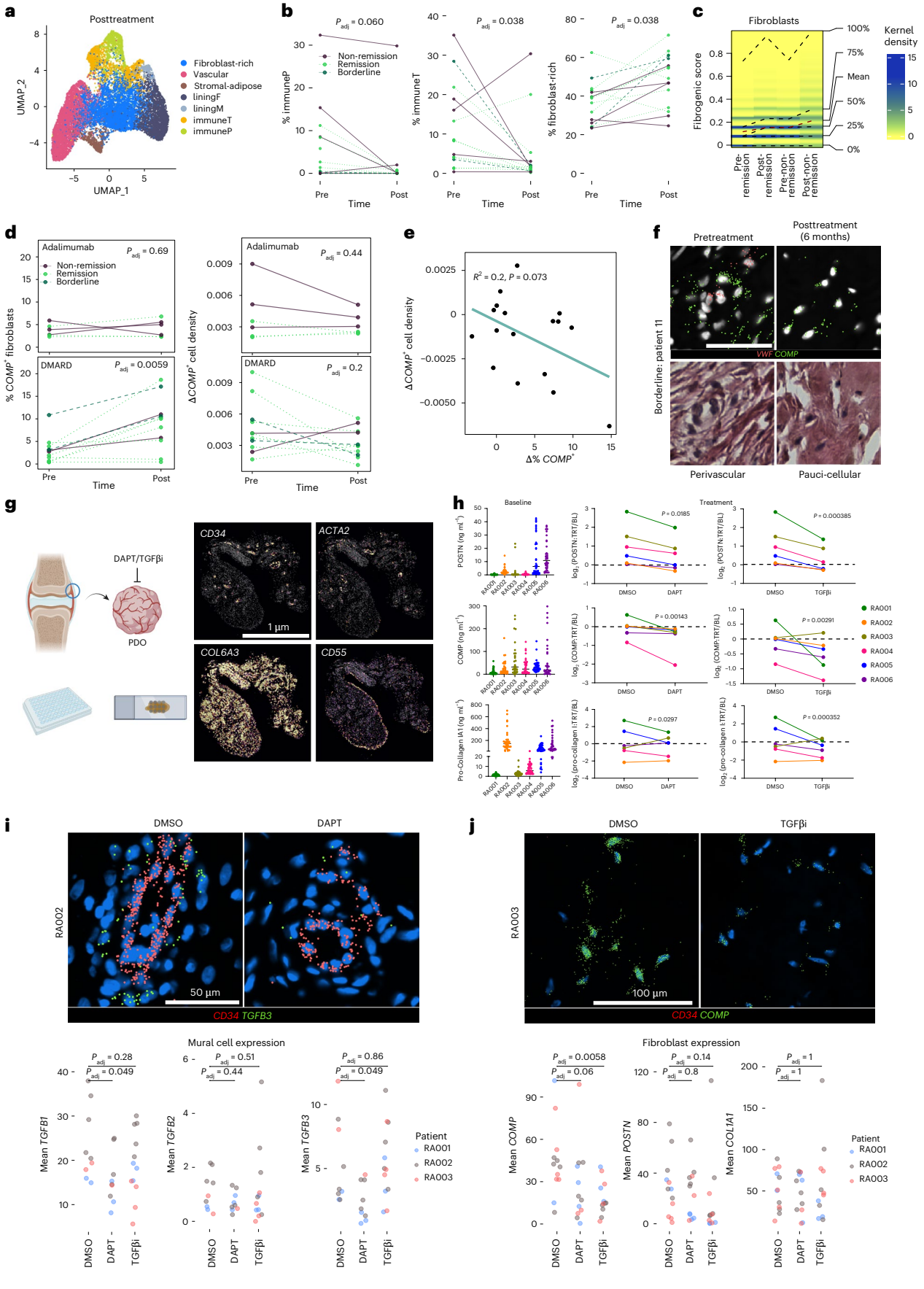

custom fibrogenic gene panel to spatially profile PDOs from three RA donors (Fig. 8i,j and Extended Data Fig. 10b–f), identifying four distinct cellular niches based on marker gene expression: vascular, lining, sublining and mural (Fig. 8g and Extended Data Fig. 10b,c). There was evidence of immune activity, although the panel was not designed to detect these populations (Extended Data Fig. 10d). To determine the effect of DAPT on perivascular TGFβ isoform and receptor expression, we examined the EC-proximal mural cell compartment where Notch signaling was most enriched (Fig. 8i and Extended Data Fig. 10e). Consistent with our observations from in vitro-cultured fibroblasts, DAPT treatment significantly suppressed *TGFB1* and *TGFB3* expression while de-repressing *TGFBR2* and *TGFBR3*. Further, per-organoid fibroblast *COMP* expression was significantly diminished by TGFβi and reduced with DAPT (Fig. 8j and Extended Data Fig. 10f). Spatially, *COMP* was most abundantly expressed in the pauci-cellular regions, where TGFβi most profoundly reversed gene expression (Fig. 8j). Collectively, our data suggest that therapeutic targeting of Notch or TGFβ signaling may abrogate fibrogenic signaling in RA synovia.

Discussion

Treatment failures in RA lead to high costs for society and cause undesirable morbidity associated with immunosuppression. Several factors have been suggested to contribute to RA treatment failure[3], yet no novel therapeutically targetable mechanism has been identified. Our study defined a Notch–TGFβ-driven fibrogenic transcriptional program associated with non-remission in RA, consistent with previous studies that have suggested an association between the expansion of synovial fibroblasts and refractory RA[15,17,39]. By implicating Notch signaling in regulating fibroblast TGFβ activity, our results provide a molecular driver of synovial tissue fibrosis in RA.

Notch is an evolutionarily conserved pathway by which cells generate boundaries within tissue[40]. In fibroblasts, we previously reported an essential role of Notch signaling in the determination of vascular fibroblast positional identity[9]. Our results demonstrate that Notch tightly regulates TGFβ receptor signaling in the perivascular compartment. Our model further suggests that the border between mural cells and fibroblasts is actively maintained via constant Notch signaling from the endothelium and that disruption of stable Notch signaling resensitizes perivascular fibroblasts to TGFβ signaling, generating the fibrogenic niche. In this model, fibrosis occurs when the tissue senses a loss of vascularity through reduced Notch signaling.

Consistent with previous studies of RA synovia, we find substantial immune depletion after treatment. However, we find this occurs whether patients achieve remission or not, suggesting that reducing the immune compartment alone is not sufficient to achieve clinical remission. Several recent studies have highlighted pain sensing as an important feature of synovial biology[41,42]. In our cohort, pain and tender joint count, rather than inflammatory components, were the drivers of sustained disease activity, thereby linking fibrogenic fibroblast populations to lack of clinical response in pain parameters. Further, we hypothesize that the subpopulation of patients who achieved remission at 6 months but still showed increased *COMP* expression may have a higher risk of relapse compared to patients with stable levels. This is consistent with our finding that baseline *COMP* transcript abundance correlated with 12-month DAS28-ESR across remission groups, and that the *COMP*$^{+}$ fibroblast population coexpresses genes such as *DKK3* previously described in patients who were refractory to multiple lines of therapy[17]. A validation study with a larger cohort and longitudinal data by the Accelerating Medicines Partnership Autoimmune and Immune-Mediated Disease (AMP-AIM) network is underway to address changes in synovial tissue in response to treatment.

Based on our findings, targeting fibrogenic activation and endothelial–fibroblast cross-talk may interrupt synovial tissue fibrosis and prevent refractory RA. Specifically, our study implicates TGFβ3 and TGFβRIII as spatially regulated components of TGFβ signaling that drive differential TGFβ response in fibroblasts. Of note, therapeutic targeting of TGFβ3 by anti-TGFβ3 antibody attenuated fibrosis in an animal model of fibrosis[43], raising the possibility of selectively targeting TGFβ3 as an adjuvant therapy to prevent exuberant synovial tissue fibrosis in RA patients.

Online content

Any methods, additional references, Nature Portfolio reporting summaries, source data, extended data, supplementary information, acknowledgements, peer review information; details of author contributions and competing interests; and statements of data and code availability are available at https://doi.org/10.1038/s41590-025-02386-2.

References

1. Gravallese, E. M. & Firestein, G. S. Rheumatoid arthritis - common origins, divergent mechanisms. *N. Engl. J. Med.* **388**, 529–542 (2023).
2. Smolen, J. S., Aletaha, D. & McInnes, I. B. Rheumatoid arthritis. *Lancet* **388**, 2023–2038 (2016).
3. Nagy, G. et al. EULAR definition of difficult-to-treat rheumatoid arthritis. *Ann. Rheum. Dis.* **80**, 31–35 (2021).
4. Hofman, Z. L. M. et al. Difficult-to-treat rheumatoid arthritis: what have we learned and what do we still need to learn? *Rheumatology* **64**, 65–73 (2025).
5. Chatzidionysiou, K. & Sfikakis, P. P. Low rates of remission with methotrexate monotherapy in rheumatoid arthritis: review of randomised controlled trials could point towards a paradigm shift. *RMD Open* **5**, e000993 (2019).
6. Qi, W. et al. Characteristics of patients with difficult-to-treat rheumatoid arthritis: a descriptive retrospective cohort study. *Adv. Rheumatol.* **64**, 55 (2024).
7. Buckley, C. D., Ospelt, C., Gay, S. & Midwood, K. S. Author Correction: Location, location, location: how the tissue microenvironment affects inflammation in RA. *Nat. Rev. Rheumatol.* **17**, 246 (2021).
8. Mizoguchi, F. et al. Functionally distinct disease-associated fibroblast subsets in rheumatoid arthritis. *Nat. Commun.* **9**, 789 (2018).
9. Wei, K. et al. Notch signalling drives synovial fibroblast identity and arthritis pathology. *Nature* **582**, 259–264 (2020).
10. Smith, M. H. et al. Drivers of heterogeneity in synovial fibroblasts in rheumatoid arthritis. *Nat. Immunol.* **24**, 1200–1210 (2023).
11. Zhang, F. et al. Defining inflammatory cell states in rheumatoid arthritis joint synovial tissues by integrating single-cell transcriptomics and mass cytometry. *Nat. Immunol.* **20**, 928–942 (2019).
12. Croft, A. P. et al. Distinct fibroblast subsets drive inflammation and damage in arthritis. *Nature* **570**, 246–251 (2019).
13. Rauber, S. et al. CD200 fibroblasts form a pro-resolving mesenchymal network in arthritis. *Nat. Immunol.* **25**, 682–692 (2024).
14. Weinand, K. et al. The chromatin landscape of pathogenic transcriptional cell states in rheumatoid arthritis. *Nat. Commun.* **15**, 4650 (2024).
15. Zhang, F. et al. Deconstruction of rheumatoid arthritis synovium defines inflammatory subtypes. *Nature* **623**, 616–624 (2023).
16. Lewis, M. J. et al. Molecular portraits of early rheumatoid arthritis identify clinical and treatment response phenotypes. *Cell Rep.* **28**, 2455–2470 (2019).
17. Rivellese, F. et al. Rituximab versus tocilizumab in rheumatoid arthritis: synovial biopsy-based biomarker analysis of the phase 4 R4RA randomized trial. *Nat. Med.* **28**, 1256–1268 (2022).
18. Distler, J. H. W. et al. Shared and distinct mechanisms of fibrosis. *Nat. Rev. Rheumatol.* **15**, 705–730 (2019).
19. Frangogiannis, N. Transforming growth factor-β in tissue fibrosis. *J. Exp. Med.* **217**, e20190103 (2020).

20. Remst, D. F. G., Blaney Davidson, E. N. & van der Kraan, P. M. Unravelling osteoarthritis-related synovial fibrosis: a step closer to solving joint stiffness. *Rheumatology* **54**, 1954–1963 (2015).
21. Korsunsky, I. et al. Cross-tissue, single-cell stromal atlas identifies shared pathological fibroblast phenotypes in four chronic inflammatory diseases. *Med.* **3**, 481–518 (2022).
22. Raza, K., Buckley, C. E., Salmon, M. & Buckley, C. D. Treating very early rheumatoid arthritis. *Best Pract. Res. Clin. Rheumatol.* **20**, 849–863 (2006).
23. Stein, D. J., Tran, M. & Korsunsky, I. Accurate tiling of spatial single-cell data with Tessera. Preprint at *bioRxiv* https://doi.org/10.1101/2025.01.17.633630 (2025).
24. Humby, F. et al. Synovial cellular and molecular signatures stratify clinical response to csDMARD therapy and predict radiographic progression in early rheumatoid arthritis patients. *Ann. Rheum. Dis.* **78**, 761–772 (2019).
25. Nerviani, A. et al. A pauci-immune synovial pathotype predicts inadequate response to TNFα-blockade in rheumatoid arthritis patients. *Front. Immunol.* **11**, 845 (2020).
26. Lliso-Ribera, G. et al. Synovial tissue signatures enhance clinical classification and prognostic/treatment response algorithms in early inflammatory arthritis and predict requirement for subsequent biological therapy: results from the pathobiology of early arthritis cohort (PEAC). *Ann. Rheum. Dis.* **78**, 1642–1652 (2019).
27. Crossin, K. L. & Krushel, L. A. Cellular signaling by neural cell adhesion molecules of the immunoglobulin superfamily. *Dev. Dyn.* **218**, 260–279 (2000).
28. Cavender, D. et al. Pathways to chronic inflammation in rheumatoid synovitis. *Fed. Proc.* **46**, 113–117 (1987).
29. Tsukui, T., Wolters, P. J. & Sheppard, D. Alveolar fibroblast lineage orchestrates lung inflammation and fibrosis. *Nature* **631**, 627–634 (2024).
30. Patrick, R. et al. Integration mapping of cardiac fibroblast single-cell transcriptomes elucidates cellular principles of fibrosis in diverse pathologies. *Sci. Adv.* **10**, eadk8501 (2024).
31. Tabib, T. et al. Myofibroblast transcriptome indicates SFRP2 fibroblast progenitors in systemic sclerosis skin. *Nat. Commun.* **12**, 4384 (2021).
32. Adams, T. S. et al. Single-cell RNA-seq reveals ectopic and aberrant lung-resident cell populations in idiopathic pulmonary fibrosis. *Sci. Adv.* **6**, eaba1983 (2020).
33. Gur, C. et al. LGR5 expressing skin fibroblasts define a major cellular hub perturbed in scleroderma. *Cell* **185**, 1373–1388 (2022).
34. Zhu, H. et al. Fibroblast subpopulations in systemic sclerosis: functional implications of individual subpopulations and correlations with clinical features. *J. Invest. Dermatol.* **144**, 1251–1261 (2024).
35. Wieteska, Ł et al. Structures of TGF-β with betaglycan and signaling receptors reveal mechanisms of complex assembly and signaling. *Nat. Commun.* **16**, 1778 (2025).
36. Heldin, C. -H. & Moustakas, A. Signaling receptors for TGF-β family members. *Cold Spring Harb. Perspect. Biol.* **8**, a022053 (2016).
37. Nichol, D. & Stuhlmann, H. EGFL7: a unique angiogenic signaling factor in vascular development and disease. *Blood* **119**, 1345–1352 (2012).
38. Mangoni, A. A. & Zinellu, A. Periostin and rheumatic diseases: early insights from a systematic review and meta-analysis. *Clin. Exp. Med.* **25**, 75 (2025).
39. Micheroli, R. et al. Role of synovial fibroblast subsets across synovial pathotypes in rheumatoid arthritis: a deconvolution analysis. *RMD Open* **8**, e001949 (2022).
40. Bray, S. J. Notch signalling in context. *Nat. Rev. Mol. Cell Biol.* **17**, 722–735 (2016).
41. Bai, Z. et al. Synovial fibroblast gene expression is associated with sensory nerve growth and pain in rheumatoid arthritis. *Sci. Transl. Med.* **16**, eadk3506 (2024).
42. Hasegawa, T. et al. Macrophages and nociceptor neurons form a sentinel unit around fenestrated capillaries to defend the synovium from circulating immune challenge. *Nat. Immunol.* **25**, 2270–2283 (2024).
43. Sun, T. et al. Isoform-selective TGF-β3 inhibition for systemic sclerosis. *Med.* **5**, 132–147 (2024).

Kartik Bhamidipati[1,20], Alexa B. R. McIntyre[1,2,20], Shideh Kazerounian[1], Gao Ce[1], Soon W. Wong[3,4], Miles Tran[1], Sean A. Prell[1], Rachel Lau[5,6], Vikram Khedgikar[1], Christopher Altmann[3,4], Annabelle Small[3,4], Roopa Madhu[7], Sonia R. Presti[1], Ksenia S. Anufrieva[1], Philip E. Blazar[8], Jeffrey K. Lange[8], Jennifer A. Seifert[9], Accelerating Medicines Partnership RA/SLE Network*, Accelerating Medicines Partnership: Autoimmune and Immune-Mediated Diseases Network (AMP-AIM)*, Colorado Interdisciplinary Joint Biology Program (CUIJBP) Consortium*, Larry W. Moreland[9], Adam P. Croft[10,11], Melanie H. Smith[12,13], Laura T. Donlin[12,13], Myles J. Lewis[5,6], Anna H. Jonsson[9], Costantino Pitzalis[5,6], Ranjeny Thomas[14], Ellen M. Gravallese[1], Michael B. Brenner[1], Ilya Korsunsky[1,7,15,16], Mihir D. Wechalekar[3,4,21] & Kevin Wei[1,21] ✉

[1]Division of Rheumatology, Inflammation, and Immunity, Brigham and Women's Hospital at Harvard Medical School, Boston, MA, USA. [2]Division of Molecular Medicine and Virology, Linköping University, Linköping, Sweden. [3]College of Medicine and Public Health, Flinders University, Adelaide, South Australia, Australia. [4]Department of Rheumatology, Flinders Medical Centre, Bedford Park, South Australia, Australia. [5]Centre for Experimental Medicine and Rheumatology, EULAR Centre of Excellence, William Harvey Research Institute, Queen Mary University of London, London, UK. [6]Barts Health NHS Trust, Barts Biomedical Research Centre (BRC), National Institute for Health and Care Research (NIHR), London, UK. [7]Division of Genetics, Brigham and Women's Hospital at Harvard Medical School, Boston, MA, USA. [8]Department of Orthopedic Surgery, Brigham and Women's Hospital, Boston, MA, USA. [9]Division of Rheumatology, The University of Colorado Anschutz Medical Campus, Aurora, CO, USA. [10]Rheumatology Research Group, Department of

Inflammation and Ageing, College of Medicine & Health, University of Birmingham, Birmingham, UK. [11]NIHR Birmingham Biomedical Research Center and Clinical Research Facility, Queen Elizabeth Hospital, University of Birmingham, Birmingham, UK. [12]Hospital for Special Surgery, New York, NY, USA. [13] Weill Cornell Medicine, New York, NY, USA. [14]Frazer Institute, The University of Queensland, Woolloongabba, Queensland, Australia. [15]Broad Institute of Massachusetts Institute of Technology (MIT) and Harvard, Cambridge, MA, USA. [16]Department of Biomedical Informatics, Harvard Medical School, Boston, MA, USA. [20]These authors contributed equally: Kartik Bhamidipati, Alexa B. R. McIntyre. [21]These authors jointly supervised this work: Kevin Wei, Mihir D. Wechalekar. *Lists of authors and their affiliations appear at the end of the paper. ✉e-mail: kwei@bwh.harvard.edu

Accelerating Medicines Partnership RA/SLE Network

Jennifer A. Seifert[9], Larry W. Moreland[9], Anna H. Jonsson[9], Laura T. Donlin[12], Costantino Pitzalis[5,6], Ellen M. Gravallese[1], Michael B. Brenner[1] & Kevin Wei[1,21]

Accelerating Medicines Partnership: Autoimmune and Immune-Mediated Diseases Network (AMP-AIM)

Jennifer A. Seifert[9], Larry W. Moreland[9], Anna H. Jonsson[9], Laura T. Donlin[12,14], Melanie H. Smith[12,14], Costantino Pitzalis[5,6], Ellen M. Gravallese[1], Michael B. Brenner[1], Kevin Wei[1,21], Roopa Madhu[7], Ranjeny Thomas[15] & Mihir D. Wechalekar[3,4,21]

Colorado Interdisciplinary Joint Biology Program (CUIJBP) Consortium

Larry W. Moreland[9], Michael J. Zuscik[17], Jennifer A. Seifert[9], Michael R. Clay[18], Andrew D. Clauw[9], Melissa Griffith[9], Terrin Geohring[17], Anna H. Jonsson[9], Patrick M. Carry[17,19], V. Michael Holers[9], Cherl L. Ackert-Bicknell[17], Daniel Moon[17], Craig A. Hogan[17], Rachel M. Frank[17], Michael R. Dayton[17], Fraser J. Leversedge[17] & Adam J. Seidl[17]

[17]Department of Orthopedics, University of Colorado, Aurora, CO, USA. [18]Department of Pathology, University of Colorado Anschutz, Aurora, CO, USA. [19]The Musculoskeletal Research Center, Children's Hospital Colorado, Aurora, CO, USA.

Methods

Human clinical samples

RA synovial tissue was obtained from patient donors at the Flinders Medical Center and was approved by the Southern Adelaide Clinical Human Research Ethics Committee (protocol no. 396.10), the Mass General Brigham Human Research Committee (IRB 2019P002924), the Colorado Multiple Institutional Review Board (IRB 20-1908) and Hospital for Special Surgery (IRB 2014-233). Samples were obtained via synovial biopsy or retrieved from patients with RA who were undergoing arthroplasty or synovectomy and were formalin-fixed and paraffin-embedded (FFPE) or OCT-embedded immediately after retrieval. RA synovial biopsy samples were retrieved using the small-bore arthroscopic method on active joints under direct vision. A biopsy was performed on the same joint at baseline and 6 months. Clinical characteristics of patients are available in Supplementary Table 1. Enrollment complied with relevant ethical regulations of all institutions. Informed consent was obtained from all participants.

Xenium slide preparation

FFPE blocks were sliced onto Xenium slides according to the Xenium In Situ for FFPE Tissue Preparation Guide (CG000578 Rev C, 10x Genomics) protocol. The Xenium slides were then prepared following the Xenium In Situ for FFPE-Deparaffinization and Decrosslinking protocol (CG000580 Rev D, 10x Genomics). In brief, the slides were baked at 60 °C for 30 min and then sequentially immersed in xylene, ethanol and nuclease-free water to deparaffinize and rehydrate the tissue. Immediately after, the Xenium slides were incubated in the decrosslinking and permeabilization solution at 80 °C for 30 min, followed by a wash with PBS-T.

For co-cultures, Xenium slides were precoated with diluted 1:10 diluted Matrigel (Corning, 356231) after which a mixture of fibroblasts (120,000) and HUVECs (60,000) were seeded for 72 h. Slides were fixed and permeabilized according to protocols for fresh frozen tissue (CG000581).

Next, the slides were prepared according to the Xenium Prime In Situ Gene Expression user guide (CG000760 Rev A, 10x Genomics) for the remaining steps or Xenium In Situ Gene Expression - Probe Hybridization, Ligation & Amplification (CG000582) for co-culture. Probes from the Xenium Prime 5 K Human Pan Tissue & Pathways Panel (PN-1000671, 10x Genomics) and the custom add-on panels were hybridized to the samples at 50 °C for 18 h. After hybridization, the slides underwent washing, incubation with a ligation reaction mix, another wash step and DNA amplification. Finally, cell segmentation staining was conducted, and the slides were treated with an autofluorescence quencher and DAPI before being loaded into the Xenium instrument.

Xenium Analyzer setup and data acquisition

Processed Xenium slides were loaded in the Xenium Analyzer and imaged, following the guidelines in the Xenium Analyzer User Guide (CG000584 Rev F, 10x Genomics). After scanning, the Xenium slides were removed from the Xenium Analyzer, and processed with post-run H&E staining according to the Xenium In Situ Gene Expression - Post-Xenium Analyzer H&E Staining protocol (CG000613 Rev A, 10x Genomics).

Xenium data cell typing and niche analysis

Cells in Xenium data were segmented using Xenium Onboard Analysis, based on nuclear expansion (custom panel co-culture data) or multimodal cell segmentation using cell boundary, interior and nuclear stains (5k data).

Single-cell and niche analysis were performed using Seurat v5.0.0 after filtering out cells with ≤50 transcript species ('nFeatures') and log normalizing data for each sample with the median transcripts detected as the scale factor. Single cells from different samples were integrated using Harmony[44]. Niches were identified using Tessera[23] based on Harmony embeddings. We labeled cell types and niches in 5,101-gene panel data based on the enrichment of marker genes associated with co-clustering cells or niches. For cell types, neighbor detection and UMAP were run with 20 principal components, and clustering with a resolution of 0.3. For niches, neighbor detection and UMAP were run with 10 principal components, and clustering with a resolution of 0.2. Example niches were selected among the top three most typical (by Euclidean distance to the average cell-type representation) within a single sample in which all niches were detected. In some cases, Xenium Explorer v3.2 was used for visualization of transcripts.

For the 50-gene custom panel data, endothelial and mural cells were identified based on enrichment of markers (*PECAM1* and *ACTA2*, respectively) in clustered data. For comparison to *COMP*$^{+}$ fibroblasts, fibroblasts were identified based on expression of *PDGFRB* and *NOTCH2* > 0 and exclusion from endothelial and mural cell clusters.

Transcript kernel density estimate analysis

We calculated kernel density estimates using the tidy_kde function from the eks R package[45]. Pairwise Pearson correlations were calculated by taking density values for different transcripts at each pixel within a sample, after selecting for subregions on the slide based on 50% contour regions of the *COL1A1* kernel density estimate or regions with DAPI above background, as specified. For *COMP*^{hi} regions in Fig. 7, we considered cell counts per area within regions defined by the 50% contour region of the kernel density estimate per sample. We used the R packages terra and raster to mask subregions.

scRNA-seq analysis

For analysis of scRNA-seq data, we used the R package Seurat v5.0 for downstream analysis. The filtered count matrix was used as input, and we used SCTransform to normalize data before principal coordinate analysis and UMAP projection. Differential expression analysis was performed using the FindMarkers function with a Wilcoxon test and gene signature scores were applied to datasets using the AddModuleScore_Ucell function from the UCell package. The DotPlot function was used to generate bubble plots depicting the expression of indicated genes across cell populations and the VlnPlot function was used to generate violin plots.

Immunofluorescence

OCT-embedded synovial sections were equilibrated at −20 °C for 10 min, and 10-m sections were obtained using a cryostat, mounted onto a glass slide and stored at −80 °C. Before staining, slides were equilibrated for 5 min at 20 °C, sections were encircled with a PAP pen (ImmEdge, Vector Labs), rehydrated with PBS for 5 min at 20 °C, fixed for 10 min in 4% paraformaldehyde, washed three times with PBS, and blocked for 1 h in TBS-T with 5% BSA and 0.2% Triton X-100. The following primary antibodies were diluted in blocking buffer and incubated overnight at 4 °C: phospho-SMAD3 (Thermo Fisher Scientific; 1:200 dilution), TGFβ1 (Thermo Fisher Scientific; 1:100 dilution), TGFβ2 (Thermo Fisher Scientific; 1:50 dilution), TGFβ3 (Thermo Fisher Scientific; 1:100 dilution), NOTCH3-PE (BioLegend; 1:50 dilution), CD45-FITC (BioLegend; 1:50 dilution), collagen I (Thermo Fisher Scientific; 1:1,000 dilution) and vWF (Thermo Fisher Scientific; 1:100 dilution). Primary antibodies were removed, and sections were washed with PBS-T three times before secondary antibody incubation with the following antibodies at a 1:500 dilution in blocking buffer: AF660 anti-mouse (Thermo Fisher Scientific, A-21074) and AF555 anti-rabbit (Thermo Fisher Scientific; A-21424). Secondary antibodies were removed, sections were washed three times with PBS-T and mounted using Fluoromount-G mounting medium with DAPI (Thermo Fisher Scientific). Images were acquired on an EVOS M7000.

In vitro culture

Synovial fibroblast cell lines were thawed and cultured in DMEM supplemented with 10% FBS, 10 mM HEPES, 1% MEM amino acids, 1%

non-essential amino acids, 1% L-glutamine, 1% penicillin–streptomycin, 55 µM β-mercaptoethanol and 1% gentamicin (pH 7.4). HUVECs (Thermo Fisher Scientific) were thawed and maintained in EGM-Plus media supplemented with the EGM-plus bulletkit (Lonza). Passages 3 to 6 were used for experiments. For DLL4 stimulation experiments, cell culture plates were precoated overnight with 5 µg ml^{-1} DLL4-Fc (R&D Systems) and for co-cultures, plates were precoated overnight with a 1:10 dilution of Matrigel (Corning, 356231) and washed with PBS. In some conditions, cells were treated with TGF beta-1 (PeproTech, 10 ng ml^{-1}), DAPT (Selleckchem, 10 µM) or TGFβ inhibitor (SB431542, 10 µM) or antibodies against TGFβ isoforms (Proteintech a-TGFβ1 69012-1-Ig; Thermo Fisher Scientific a-TGFβ1,2,3 MA5-23795, R&D Systems a-TGFβ2 AB-12-NA, R&D Systems a-TGFβ3 MAB243) at a concentration of 5 µg ml^{-1}. The following siRNAs (Thermo Fisher Scientific) were added to monocultures or co-cultures at a 20 nM concentration at the start of cultures and were re-dosed every 72 h, when applicable: *NTC* (4390843), *JAG1* (s1174) and *DLL4* (s534448), *TGFB1* (s14054), *TGFB2* (s14059), *TGFB3* (s224725), *TGFBR1* (s14073), *TGFBR2* (s14077) and *TGFBR3* (s24). siRNA treatment was performed as described in the Lipofectamine RNAiMax protocol (Thermo Fisher Scientific). For RT–qPCR experiments, 10,000 fibroblasts were seeded in 96 wells. For immunoblotting, 250,000 fibroblasts were seeded in six-well plates before stimulation and cell lysis. For co-cultures, a fixed number of fibroblasts (5,000) were cultured with HUVECs (5,000) at a 1:1 ratio, unless otherwise indicated in the figure legends.

Flow cytometry

Fibroblasts or co-cultures were trypsinized and directly stained with an equal volume of primary antibody solution (Cell staining buffer, BioLegend) containing eFluor 780 Fixable Viability Dye (Thermo Fisher Scientific; 1:1,000 dilution), TGFβR2-APC (BioLegend; 1:100 dilution), TGFβRIII (Proteintech, 20000-1-AP; 1:100 dilution) or CD31-FITC (BioLegend; 1:100 dilution) for 30 min at 4 C. Cells were washed with cell staining buffer (BioLegend), fixed in 4% paraformaldehyde for 10 min at 20 °C, washed, and stained with AF555 anti-rabbit (Thermo Fisher Scientific) for 30 min at 4 °C for detection of TGFβIII. Cells were washed and resuspended in cell staining buffer. PDOs after 4 days of culture were disaggregated in RPMI 1640 medium (Thermo Fisher Scientific) containing Liberase TL (100 µg ml^{-1}; Sigma Aldrich) and DNAse I (100 µg ml^{-1}; Stemcell Technologies), filtered through a 70 µm cell strainer, washed and stained as described with eflour780 Fixable viability dye, CD31-BV21 (BioLegend; 1:100 dilution), FITC-CD45 (BioLegend; 1:100 dilution) and PE-PDPN (BioLegend; 1:100 dilution) in the presence of Fc blocking reagent (BioLegend). Data were acquired on a BD FACSCanto II and further analyzed with Flowjo version 10.

RNAScope and quantification

A 3:1 ratio of fibroblasts and ECs (7500 fibroblasts, 2500 HUVECs) was seeded on Matrigel (Corning; 1:10 dilution) precoated 96-well plates (Agilent, 204626-100). After culture and treatment with siRNA for 5 days, cells were washed with PBS, fixed in 10% NBF and processed for staining and imaging according to the manufacturer's protocol with the RNAScope multiplex fluorescent V2 assay (ACD Bio, SOP 45-009 A). Images were acquired on an EVOS M7000.

Results were quantified by segmenting nuclei based on DAPI staining using Cellpose[46] and performing nuclear expansion to approximate cell boundaries. We then used scikit-image[47] to calculate mean intensities per cell.

Immunoblot

Following incubation, cells were trypsinized and rinsed with cold PBS. Cells were pelleted by centrifugation at 350*g* for 10 min. Cell pellets were resuspended in 100 µl of RIPA buffer (Thermo Fisher Scientific, 89900) supplemented with 0.1% Triton X-100, protease and phosphatase inhibitor mini-tablets (Thermo Fisher Scientific, A32961) and a phosphatase inhibitor cocktail (Active Motif, 37492). The cell lysate was briefly vortexed at high speed to dissociate aggregates, incubated on ice for 30 min, and then centrifuged at high speed for 20 min at 4 °C. Protein concentration was determined using the Pierce BCA Protein Assay Kit (Thermo Fisher Scientific, 23227). Between 30 µg and 50 µg of protein was subjected to SDS–PAGE (Bio-Rad, 1610734) and transferred to a PVDF membrane (Bio-Rad, 1704273) using the Bio-Rad TRANS-BLOT TURBO transfer system (Bio-Rad, 690BR324) with a dry transfer protocol for 30 min according to the manufacturer's instructions. Membranes were blocked for 15 min in Everyblot blocking buffer (Bio-Rad, 12010020), then incubated overnight at 4 °C with primary antibodies against TGFβ1 (Proteintech, 21898-1-AP; 1:500 dilution), TGFβ2 (Proteintech, 19999-1-AP; 1:500 dilution), TGFβ3 (Proteintech, 18942-1-AP; 1:500 dilution), TGFβR1 (RD Biosciences, AF3025; 1:300 dilution), TGFβR2 (Bioss, bs-0117R; 1:500 dilution), TGFβR3 (Cell Signaling Technology, 2519S; 1:500 dilution), GAPDH (Thermo Fisher Scientific, MA5-15738) or beta-actin (Cell Signaling Technology, 3700). Following primary antibody incubation, membranes were incubated with HRP-conjugated secondary antibodies (Thermo Fisher Scientific, anti-Rabbit, 32460, anti-Mouse, 31430, or anti-Goat, A16005) for 1 h at 20 °C. All the antibody dilutions were in Everyblot blocking buffer. Blots were developed using SuperSignal West Femto Maximum Sensitivity Substrate (Thermo Fisher Scientific, 34095) or SuperSignal West Pico PLUS Chemiluminescent Substrate (Thermo Fisher Scientific, 34577) and imaged using a Bio-Rad ChemiDoc imaging system.

Analysis of Olink data

Olink protein concentration values (NPX) from AMP RA/SLE and 396.10 cohort patients were extracted with the OlinkAnalyze package. A count matrix and a separate file with metadata indicating each patient's CTAP, remission status or clinical data were formed. The lmfit and eBayes functions from the limma package were used to identify the differential abundance of proteins in patients belonging to CTAP-EFM compared to patients classified in other CTAPs and the cor function in R was used to calculate correlations. $-\log_{10}$(unadjusted *P* values) are reported in the volcano plot and adjusted *P* values (Benjamini–Hochberg correction) are reported in the associated bar plot.

Bulk RNA-seq analysis

We analyzed both bulk RNA-seq and pseudo-bulk data from spatial transcriptomics data using DESeq2 (ref. 48).

ELISA

Supernatant was collected on the indicated days and stored at 4 °C in sealed polypropylene plates before assay by ELISA. For measurement of pro-collagen 1 alpha 1 (R&D Systems, DY6220-05), COMP (R&D Systems, DY3134) or POSTN (R&D Systems, DY3548B), TGFβ1 (R&D Systems, DY240-05), TGFβ2 (R&D Systems, DY302) and TGFβ3 (DY243) plates were incubated overnight at 4 °C with diluted capture antibody solution, washed with PBS-T and blocked for 1 h at 20 °C in blocking buffer (1% BSA in PBS). For activation of latent TGFβ into an immunoreactive form, supernatant was incubated with 1 N HCl for 10 min followed by neutralization with 1.2 N NaOH/0.5 M HEPES buffer per the manufacturer's protocols. Supernatant was diluted in a blocking buffer and incubated on plates for 2 h at 20 °C, followed by a 2-h incubation of detection antibody and 30-min incubation of HRP-Streptavidin (R&D Systems) with PBS-T washes in between. The ELISA was developed with 50 µl of TMB substrate (Thermo Fisher Scientific) and stopped after 20 min with 50 µl of 2 N sulfuric acid. Absorbance was read with a plate reader (Spectramax) at 450 nm with a 570-nm background subtraction.

qPCR

Cells were lysed in TRIzol (Thermo Fisher Scientific) and RNA was extracted per the manufacturer's protocols. cDNA was synthesized using QuantiTect Reverse Transcription Kit (Qiagen) per the

manufacturer's protocols. The qPCR mastermix was prepared using Brilliant III Ultra-Fast SYBR Green QRT-PCR Master Mix (Agilent), and samples were run on an AriaMX Real Time PCR machine (Agilent). The relative abundance of transcripts was normalized to the expression of *GAPDH* mRNA using the $2^{-\Delta\Delta CT}$ method. All primer pair sequences were obtained from Origene and synthesized by IDT.

Lentiviral transduction

TGFBR2 and *TGFBR3* plasmids (pLV[Exp]-Bsd-CMV) were ordered from VectorBuilder. 293FT cells were seeded at 6×10^5 cells in a T75 flask and incubated overnight. The next day, cells were transfected according to the manufacturer's protocol with 11.18 µg of target plasmid and 17.8 µg of packaging mix (Thermo Fisher Scientific, V53406) using Lipofectamine 3000 (Thermo Fisher Scientific, L3000015) in a T75 flask. Virus supernatants were harvested and filtered after 4 days and concentrated overnight using Peg-it virus precipitation solution (System Biosciences) according to the manufacturer's protocols. Cells were transduced with lentiviral supernatants containing polybrene (10 µg ml^{-1}) for one week, with regular media changes, followed by one week of selection with blasticidin (10 µg ml^{-1}) before use in experiments.

PDOs

Cryopreserved synovial tissue specimens were thawed in a 37 °C water bath, transferred into a solution of DMEM + 10% FBS followed by PBS. Synovial tissue fragments were subsequently transferred from PBS to a 100-mm × 15-mm Petri dish and punched with a 2-mm punch biopsy tool (Integra, 33-31-P/25) to generate organoids; a minimum of 30 organoids were generated per tissue sample. Organoids were implanted into wells of a 96-well plate that were precoated with 50 µl of Matrigel (Corning, 356231). After allowing Matrigel to polymerize for 30 min at 37 °C, 100 µl of EGM-2 media was added to each well and incubated overnight. For inhibitor treatment, all media were removed before adding 100 µl media containing DMSO, DAPT (10 µM) or TGFβi (10 µM). Supernatant before (16 h) and after (72 h) inhibitor treatment was collected for ELISA analysis. For spatial profiling, PDOs were embedded in OCT after treatment, stored at −80 °C and later sectioned onto Xenium slides (10 µM) using a cryostat.

Visium HD spatial gene expression

H&E staining and imaging were performed following the Visium HD FFPE Tissue Preparation Handbook (CG000684). Samples were then processed and sequenced following the Visium HD Spatial Gene Expression Reagent Kits User Guide (CG000685). Space Ranger version 3.0 was used for analysis. Bins (8 µm) were used for visualization of gene signatures.

3D co-culture

Fibroblast and fibroblast–endothelial 3D cultures were generated as previously described[9]. Briefly, fibroblast-only cultures consisted of 200,000 fibroblasts and fibroblast plus EC cultures contained 100,000 synovial fibroblasts and 100,000 HUVECs, which were combined in a single 35-µl droplet of Matrigel, seeded on ultralow-attachment plates (Thermo Fisher Scientific, 174930) and cultured in 1 ml EGM-2 medium replaced at indicated time points (Lonza).

Transwell assay

In total, 5,000 fibroblasts were seeded onto both 96-well Transwell inserts (0.2-µM pore) and DLL4 precoated receiver plates (Corning, 3381). After incubation for 72 h, fibroblasts in the Transwell chamber and receiver plates were lysed in TRIzol for RT–qPCR.

Statistics

Statistical tests were performed using GraphPad Prism version 10.4.1 or R version 4.4.1/4.4.2. There were no tests performed to assess normality. Differences between data that were assumed to be normally distributed were assessed using Student's two-tailed *t*-tests, and differences in data assumed to be non-normally distributed data were evaluated with Mann–Whitney *U* tests. Detailed statistical descriptions, including sample size and calculation methods, are provided in the figure legends and text. A *P* value of <0.05 was considered statistically significant.

Reporting summary

Further information on research design is available in the Nature Portfolio Reporting Summary linked to this article.

Data availability

Previously published publicly available data used in this study are available in the following repositories: systemic sclerosis scRNA-seq data (GSE195452), idiopathic pulmonary fibrosis scRNA-sequencing data (GSE136831), synovial scRNA-seq data (syn52297840), micromass organoid scRNA-seq data (https://www.immport.org; SDY1599), PEAC data (E-MTAB-6141) and RBPJ ChIP–seq data (GSE127388; ENCSR596FEL). All spatial transcriptomic data generated as part of this study are available on Zenodo: RA synovial pretreatment data: https://doi.org/10.5281/zenodo.15058262 (ref. 49). RA synovial posttreatment data: https://doi.org/10.5281/zenodo.15058715 (ref. 50). RA synovial custom fibrogenesis panel ($n = 4$ tissues) and AMP Olink matrix containing NPX values and clinical metadata: https://doi.org/10.5281/zenodo.15059437 (ref. 51). Xenium profiling of 2D co-culture: https://doi.org/10.5281/zenodo.15064564 (ref. 52). RA-ILD Lung and RA synovium Visum data, RA patient-derived organoid Xenium data, 3D co-culture Xenium Data and 396.10 Olink data: https://doi.org/10.5281/zenodo.16995699 (ref. 53). Source data are provided with this paper.

References

44. Korsunsky, I. et al. Fast, sensitive and accurate integration of single-cell data with Harmony. *Nat. Methods* **16**, 1289–1296 (2019).
45. Duong, T. Statistical visualisation of tidy and geospatial data in R via kernel smoothing methods in the eks package. *Comput. Stat.* **40**, 2825–2847 (2025).
46. Stringer, C., Wang, T., Michaelos, M. & Pachitariu, M. Cellpose: a generalist algorithm for cellular segmentation. *Nat. Methods* **18**, 100–106 (2021).
47. van der Walt, S. et al. scikit-image: image processing in Python. *PeerJ* **2**, e453 (2014).
48. Love, M. I., Huber, W. & Anders, S. Moderated estimation of fold change and dispersion for RNA-seq data with DESeq2. *Genome Biol.* **15**, 550 (2014).
49. McIntyre, A. et al. Spatial patterning of fibroblast TGFβ signaling underlies treatment resistance in rheumatoid arthritis - Xenium data (pre-treatment RA synovium) (version v1). *Zenodo* https://doi.org/10.5281/zenodo.15058262 (2025).
50. McIntyre, A. et al. Spatial patterning of fibroblast TGFβ signaling underlies treatment resistance in rheumatoid arthritis - Xenium data (post-treatment RA synovium) (version v1). *Zenodo* https://doi.org/10.5281/zenodo.15058715 (2025).
51. McIntyre, A. et al. Spatial patterning of fibroblast TGFβ signaling underlies treatment resistance in rheumatoid arthritis - Xenium data (custom panel RA synovium) (version v1). *Zenodo* https://doi.org/10.5281/zenodo.15059437 (2025).
52. McIntyre, A., Bhamidipati, K., Ce, G. & Wei, K. Spatial patterning of fibroblast TGFβ signaling underlies treatment resistance in rheumatoid arthritis - Xenium data (in vitro co-culture) (version v1). *Zenodo* https://doi.org/10.5281/zenodo.15064564 (2025).
53. Wei, K. Spatial patterning of fibroblast TGFβ signaling underlies treatment resistance in rheumatoid arthritis - Xenium data (pre-treatment RA synovium). *Zenodo* https://doi.org/10.5281/zenodo.16995699 (2025).

Acknowledgements

We thank members of the K.W., I.K. and M.B.B. labs for helpful discussions. We also appreciate the contribution of synovial samples from the Colorado Interdisciplinary Joint Biology Program (CUIJBP) consortium to this study. This work is supported by a Doris Duke Foundation Clinical Scientist Development Award, a Rheumatology Research Foundation Innovative Research Grant, a Brigham and Women's Hospital Department of Medicine - Broad Institution collaborative research award and a Brigham and Women's Hospital Llura Gund Award for Rheumatoid Arthritis Research. This work was supported by the AMP-AIM. AMP-AIM is a public–private partnership (AbbVie, Arthritis Foundation, Bristol Myers Squibb, Foundation for the National Institutes of Health, GlaxoSmithKline, Janssen Research and Development, Lupus Foundation of America, Lupus Research Alliance, Merck Sharp & Dohme, National Eye Institute, National Institute of Allergy and Infectious Diseases, National Institute of Arthritis and Musculoskeletal and Skin Diseases, National Institute of Dental and Craniofacial Research, National Institute Health Office of Research on Women's Health, Novartis, Pfizer, Sanofi, and Sjogren's Foundation, and UCB) created to develop new ways of identifying and validating promising biological targets for diagnostics and drug development. Funding was provided through grants from the National Institutes of Health. A.P.C. was supported by a Kennedy Trust for Rheumatology Research Senior Research Fellowship (KENN 19 20 06). K.W. is supported by NIH-NIAMS K08AR077037, and a Burroughs Wellcome Fund Career Awards for Medical Scientists. K.B. is supported by NIH-NIAMS T32AR007530-36.

Author contributions

Conceptualization: K.B., K.W., M.D.W. and R.T. Experimental design and data generation: K.B., S.K. and V.K. Xenium data generation and panel design: G.C., S.A.P., K.B., R.M. and V.K. Data analysis: A.B.R.M., K.B., M.T., R.L. and K.S.A. Synovial tissue acquisition: C.A., A.S., S.W.W., S.R.P., P.E.B., J.K.L., A.H.J., M.D.W., R.T., M.H.S., J.A.S., L.W.M. and L.T.D. Analysis of published data: R.L., A.B.R.M., K.B., M.J.L. and C.P. Productive scientific discussion: A.P.C., E.M.G., M.B.B. and I.K. Figure generation: K.B. and A.B.R.M. Writing original draft: K.B., A.B.R.M. and K.W. Draft reviewing and editing: all authors. Supervision: K.W. and M.D.W. Funding acquisition: K.W.

Competing interests

M.D.W. has a collaborative research agreement with Janssen Pharmaceuticals USA, although unrelated to the paper. I.K. has paid consulting and advisory roles with Mestag Therapeutics, Merck Sharp & Dohme and the Lupus Research Alliance. J.K.L. is a paid consultant for Smith and Nephew, is on the scientific advisory board for OnPoint Knee and has received royalties from Cambridge Scholars Publishing for book editing. E.M.G. is an associate editor at *New England Journal of Medicine*, receives textbook royalties from Elsevier for *Rheumatology* and receives royalties from Wolters Kluwer for *UptoDate* contributions. M.B.B. is a consultant to GSK, Third Rock Ventures, 4FO Ventures and Moderna and a consultant to and founder of Mestag Therapeutics. K.W. has a sponsored-research agreement from Merck Pharmaceuticals and 10x Genomics, and served as a consultant for Mestag Therapeutics and Santa Ana Bio. The other authors declare no competing interests.

Additional information

Extended data is available for this paper at https://doi.org/10.1038/s41590-025-02386-2.

Supplementary information The online version contains supplementary material available at https://doi.org/10.1038/s41590-025-02386-2.

Correspondence and requests for materials should be addressed to Kevin Wei.

Peer review information *Nature Immunology* thanks Joseph Arron, Matthew Buechler and Shankar Subramaniam for their contribution to the peer review of this work. Peer reviewer reports are available. Primary Handling Editor: L. A. Dempsey, in collaboration with the *Nature Immunology* team.

https://doi.org/10.1038/s41590-025-02386-2

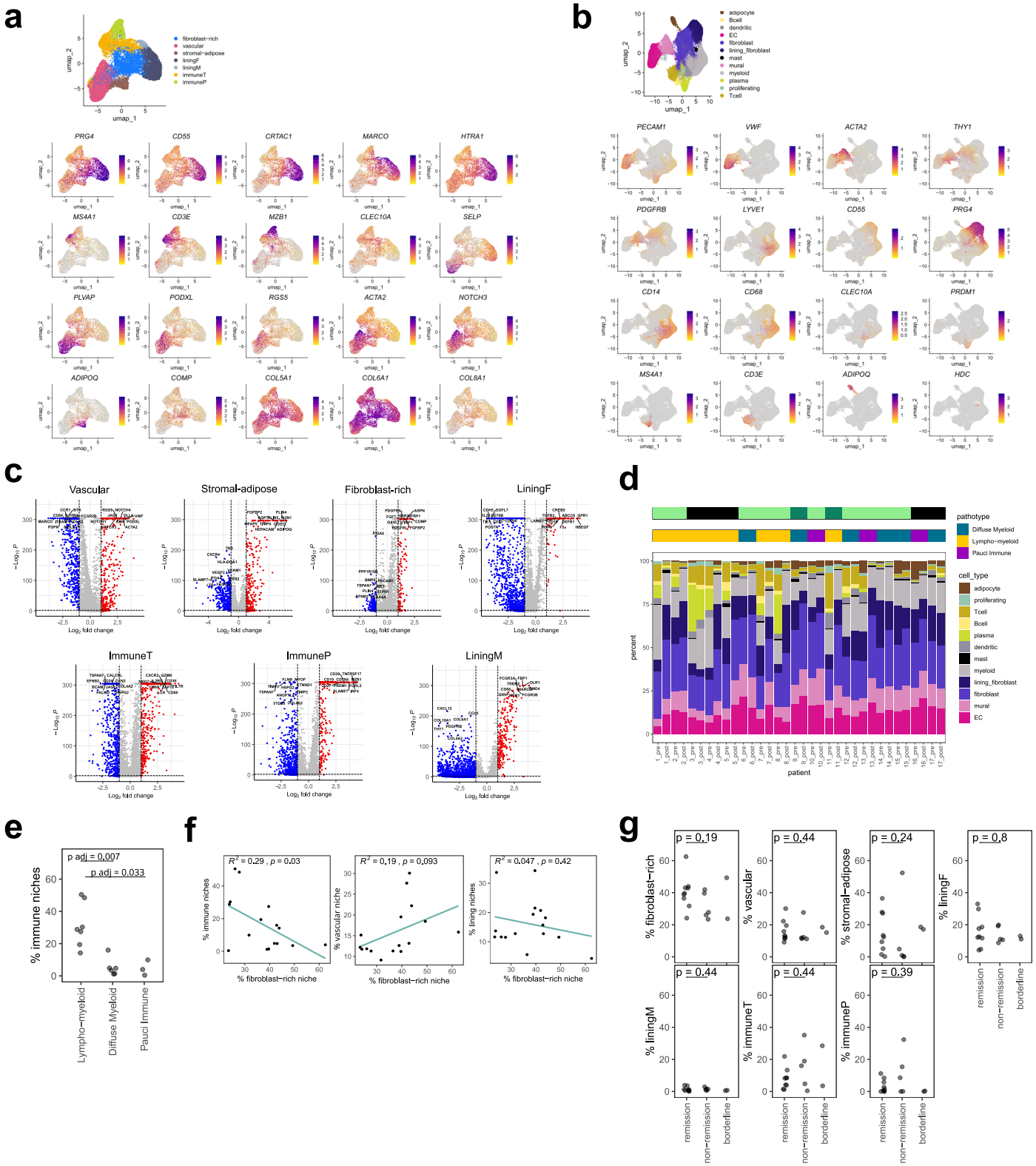

Extended Data Fig. 1 | Cell and niche analysis of pre-treatment RA synovium. **a**, UMAPs showing labelled niches (above) and niche marker genes (below). Each point represents a single niche. **b**, UMAPs showing labelled cell types (above) and cell type marker genes (below). Each point represents a single cell. **c**, Volcano plot by niche displaying marker genes. Genes in the upper right quadrant are log2 fold change > 1, padj < 0.01 for the indicated niche compared to other niches, statistics by negative binomial GLM and the Wald test; p-values are FDR-corrected **d**, Stacked bar plot summarizing cell type proportion in pre- and post-treatment samples for 17 patients. **e**, Jitter plot representing the percent area of immuneT and immuneP niches by pathotype. Statistics by two-sided Wilcoxon test with Bonferroni correction. **f**, Correlations between the percent area of each sample occupied by the fibroblast-rich versus immune, vascular or lining niches. Statistics by two-sided Pearson correlation coefficient test. **g**, Jitter plot representing the tissue area of niche in baseline biopsies by remission status. Statistics by two-sided Wilcoxon test with Bonferroni correction.

https://doi.org/10.1038/s41590-025-02386-2

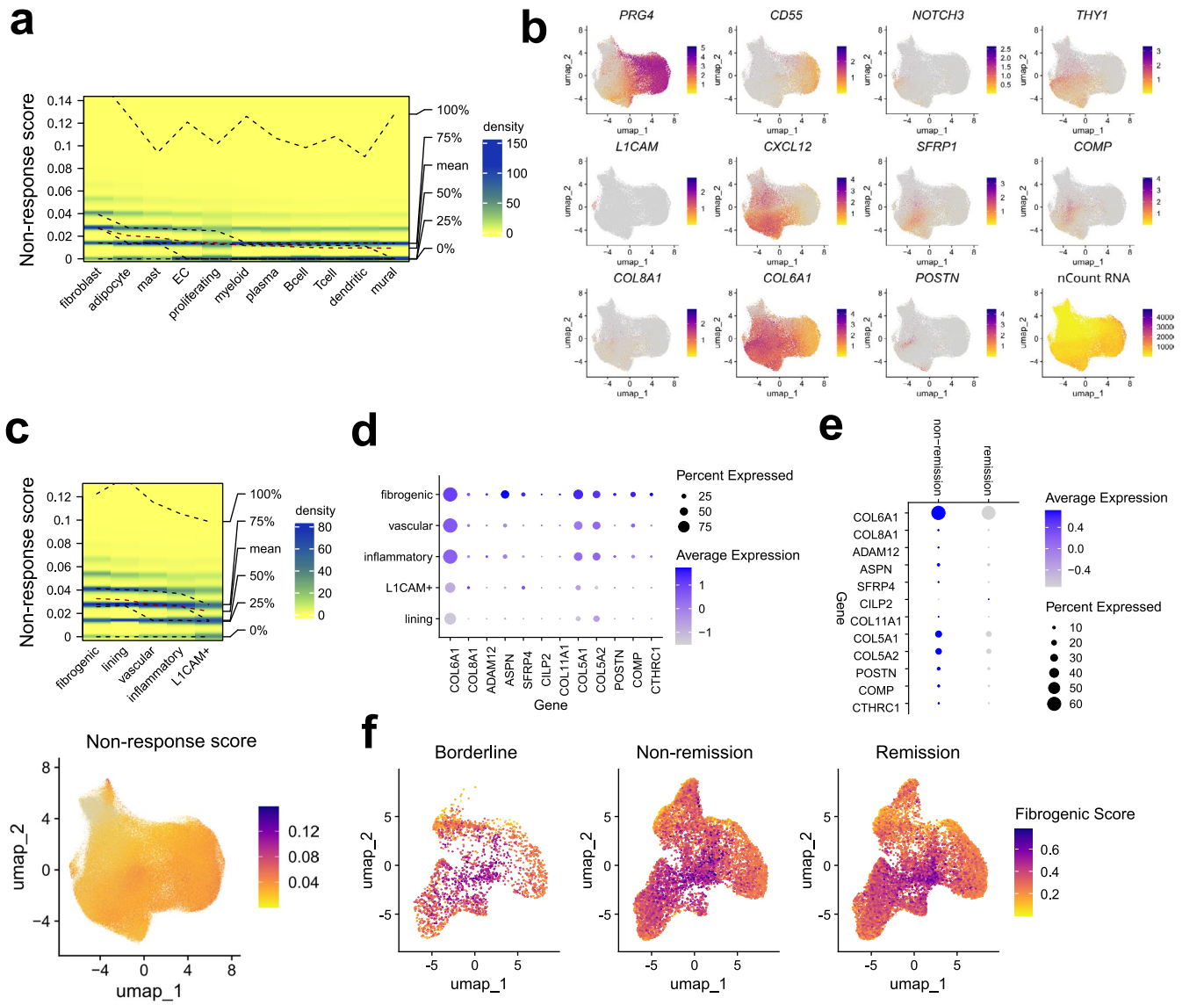

Extended Data Fig. 2 | RA fibroblast subtyping. a, Density plot showing non-response scores (UCell) by major cell lineage. The color gradient represents the frequency of cells (density) exhibiting a particular non-response score and dashed lines represent the indicated cell density percentiles by cell type. **b**, UMAP displaying markers for different fibroblast subtypes labelled in Fig. 2c. **c**, Density plot (top) showing non-response scores by fibroblast subtype and UMAP projection of non-response scores in fibroblasts (below). **d**, Dot plot representing the expression of fibrogenic markers, by fibroblast subtype. Dot plot color represents the scaled expression of genes, and the size of the dots represent the percent of cells expressing the gene. **e**, Dot plot representing the aggregate single-cell expression levels of fibrogenic genes by remission status. **f**, Niche UMAP projection of fibrogenic score separated by remission status.

https://doi.org/10.1038/s41590-025-02386-2

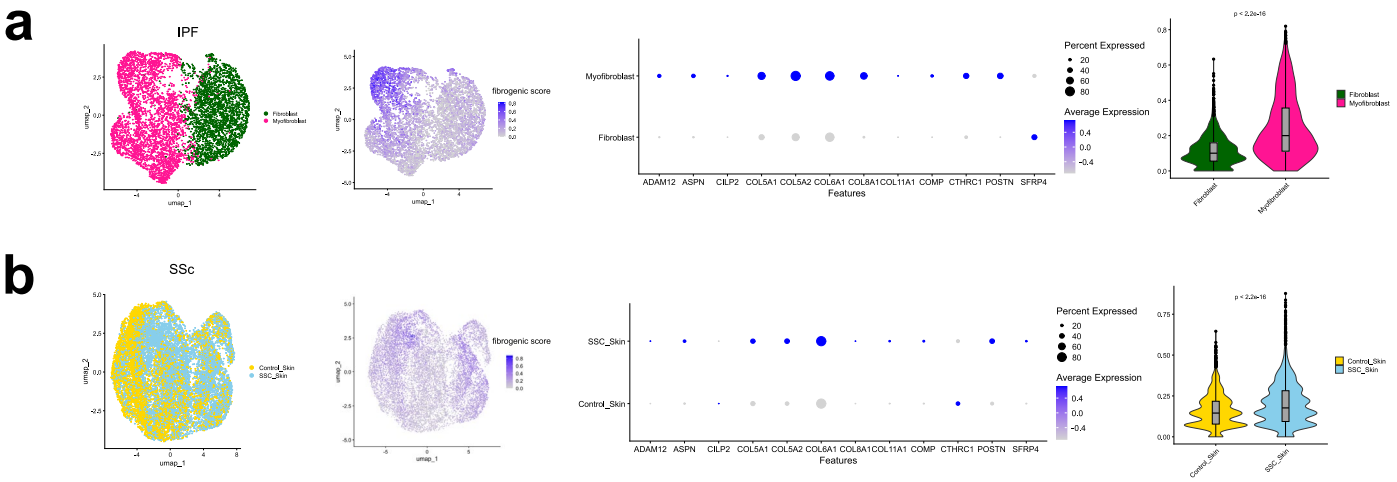

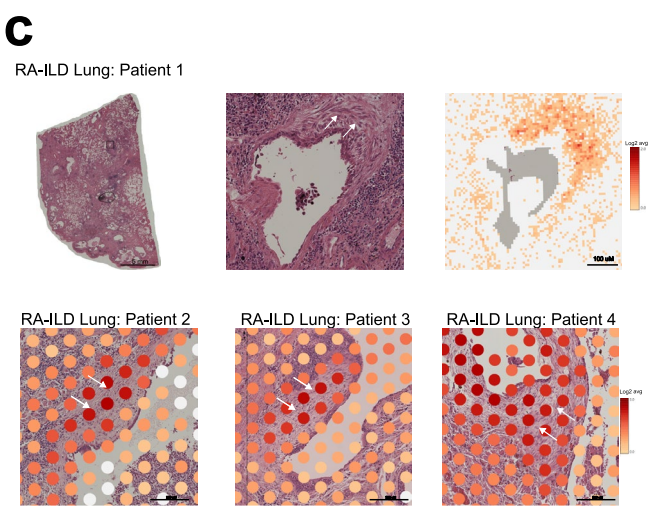

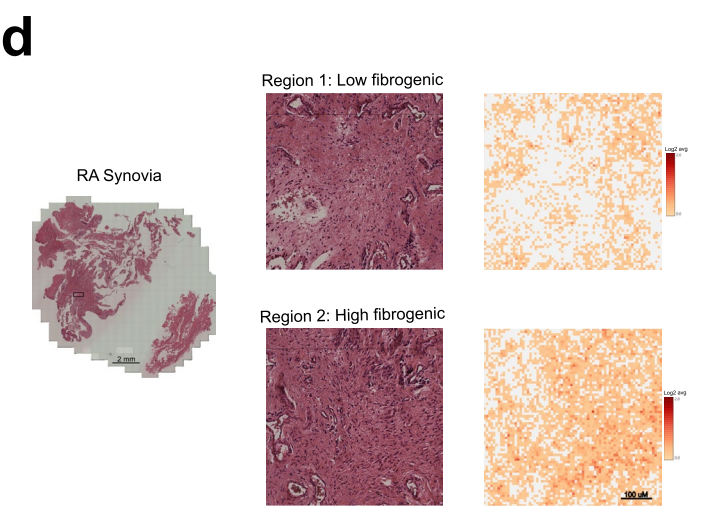

Extended Data Fig. 3 | RA fibrogenic signature in fibrotic diseases. a-b, UMAP projection of single cells from IPF and SSc datasets grouped by disease status (refs.26,27), and shaded by level of fibrogenic signature U cell score with a corresponding dot plot of genes (n = 12) that comprise the fibrogenic gene signature. Dot plot color represents the scaled expression of genes, and the size of the dots represent the percent of cells expressing the gene. Violin plot to the right displays the fibrogenic signature score, as calculated with UCell, in disease versus control samples. Two-sided Wilcoxon test was used for statistical comparisons between the groups. P < 2.2e-16 for the comparison between disease-associated and healthy fibroblasts. **c**, H&E of the whole lung section (left), region of interest (right) with arrows indicating fibroblastic foci and log2 average gene expression (Visium HD) for the fibrogenic signature genes represented in 8 µm bins. Scale bars are 5 mm and 100 µm respectively (top). Below, regions of interest in additional RA-ILD samples (Visium), scale bar 200 µm (bottom). **d**, H&E of whole RA synovial tissue section (left, scale bar 2 mm) and H&E and log2 average fibrogenic signature expression of adjacent ROIs (right, scale bare 100 µm) that display low (Region 1) and high (Region 2) fibrogenic scores respectively. **a,b** the box plots show the median and 25th–75th percentiles; the whiskers represent 1.5 times the interquartile range (IQR); outliers are shown beyond the whiskers.

https://doi.org/10.1038/s41590-025-02386-2

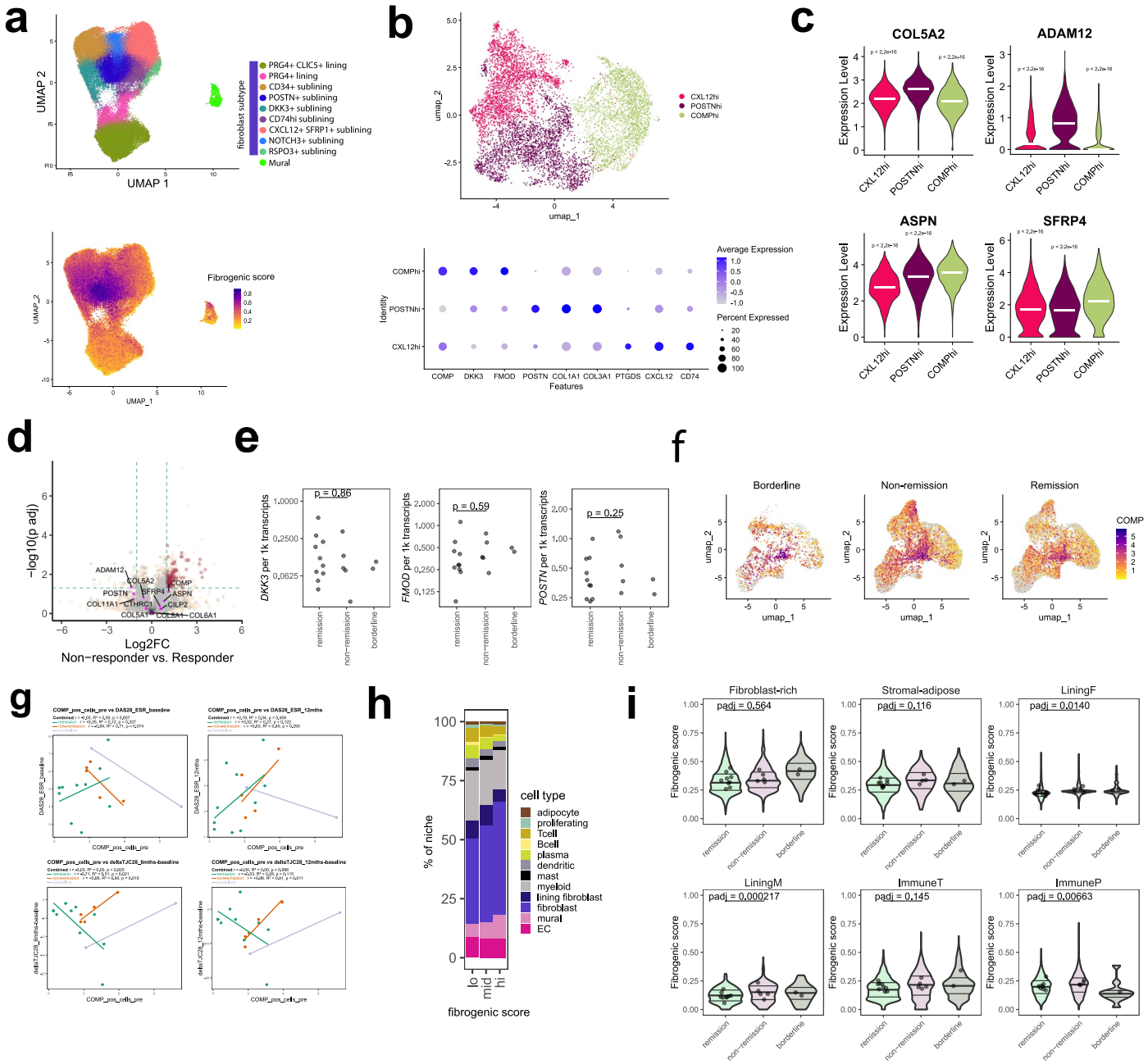

Extended Data Fig. 4 | RA fibrogenic fibroblast subtyping and quantification. **a**, UMAP projection of synovial fibroblasts with cluster annotations (top, ref.15) and projection of the fibrogenic score onto the UMAP as calculated by UCell (below). **b**, UMAP projection (top) of subsetted and re-clustered fibroblasts that had fibrogenic signature scores in the top decile. Dotplot of selected genes differentially expressed across clusters with the color representing scaled expression and size of the dot representing percent of cells expressing the gene. **c**, Violin plot of select genes differentially enriched in the *POSTN*hi versus *COMP*hi clusters with the bar representing median expression and p-values calculated using a two-sided Wilcoxon test. (Top) p < 2.2e-16 between *POSTN*hi cluster and other clusters, (Bottom) p < 2.2e-16 between *COMP*hi cluster and other clusters for indicated genes. **d**, Volcano plot representing differentially expressed genes in non-responders versus responders from bulk RNA-sequencing analysis of synovial tissue derived from treatment naïve patients. Genes in the upper right quadrant are log2 fold change > 1, padj < 0.05 between non-responders and responders. Differential expression was tested with DESeq2 (negative-binomial GLM; Wald test); p-values are FDR-corrected. Genes part of the fibrogenic signature are highlighted. **e**, Jitter plot representing normalized transcript detection of *DKK3*, *FMOD*, and *POSTN* from pre-treatment spatial transcriptomics data by response status. Statistics by two-sided Wilcoxon test. **f**, UMAP projection of *COMP* expression separated by remission status. **g**, plots showing correlation between baseline *COMP*+ cell abundance and indicated DAS28-ESR timepoint or changes in DAS28-ESR components. Statistical evaluation by two-sided Pearson correlation test. **h**, Stacked barplot representing the cell type composition of niche tiles that were classified as low ("lo"), medium ("mid") or high ("hi") for fibrogenic scores. **i**, violin plots representing the distribution of tile-level fibrogenic scores per indicated niche by remission status. The dots represent the median fibrogenic score per patient. Statistical comparison by GLM with dataset (biopsy) as a cofactor, FDR-corrected.

https://doi.org/10.1038/s41590-025-02386-2

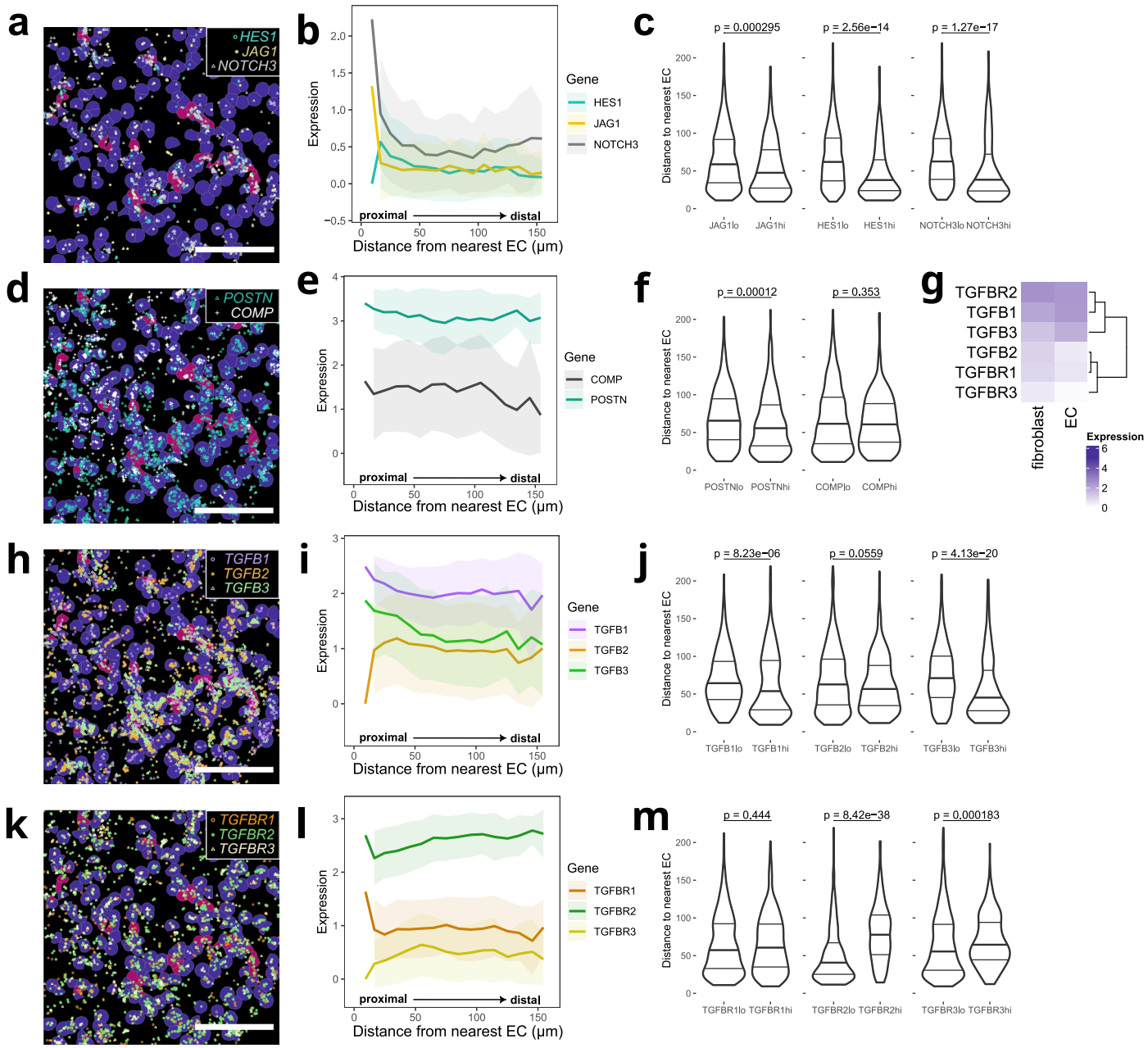

Extended Data Fig. 5 | Spatial patterning of fibroblast gene expression in 3D co-culture. a,**d**,**h**,**k** Example images of gene expression distribution overlaid on labelled cell types, to a maximum of randomly selected 1500 transcripts per gene, with Notch target genes shown in (**a**), fibrogenic markers in (**d**), *TGFB* ligands in (**h**), and *TGFB* receptors in (**k**). Scale bar indicates 200 μm. **b**,**e**,**i**,**l**, Line plot representing average expression of transcripts per fibroblast relative to the EC distance, with Notch target genes shown in (**b**), fibrogenic markers in (**e**), *TGFB* ligands in (**i**), and *TGFB* receptors in (**l**). Solid line shows mean, shaded regions show one standard deviation. **c**,**f**,**j**,**m**, Distance to the nearest EC in the top vs. bottom quantile of cells by expression of each gene, with Notch target genes shown in (**c**), fibrogenic markers in (**f**), *TGFB* ligands in (**j**), and *TGFB* receptors in (**m**). Statistics by two-sided Wilcoxon tests comparing distances from ECs for the top vs. bottom quantiles of cells in expression of each gene. **g**, Heatmap representing expression of *TGFB* ligands and receptors by cell type in the co-culture.

https://doi.org/10.1038/s41590-025-02386-2

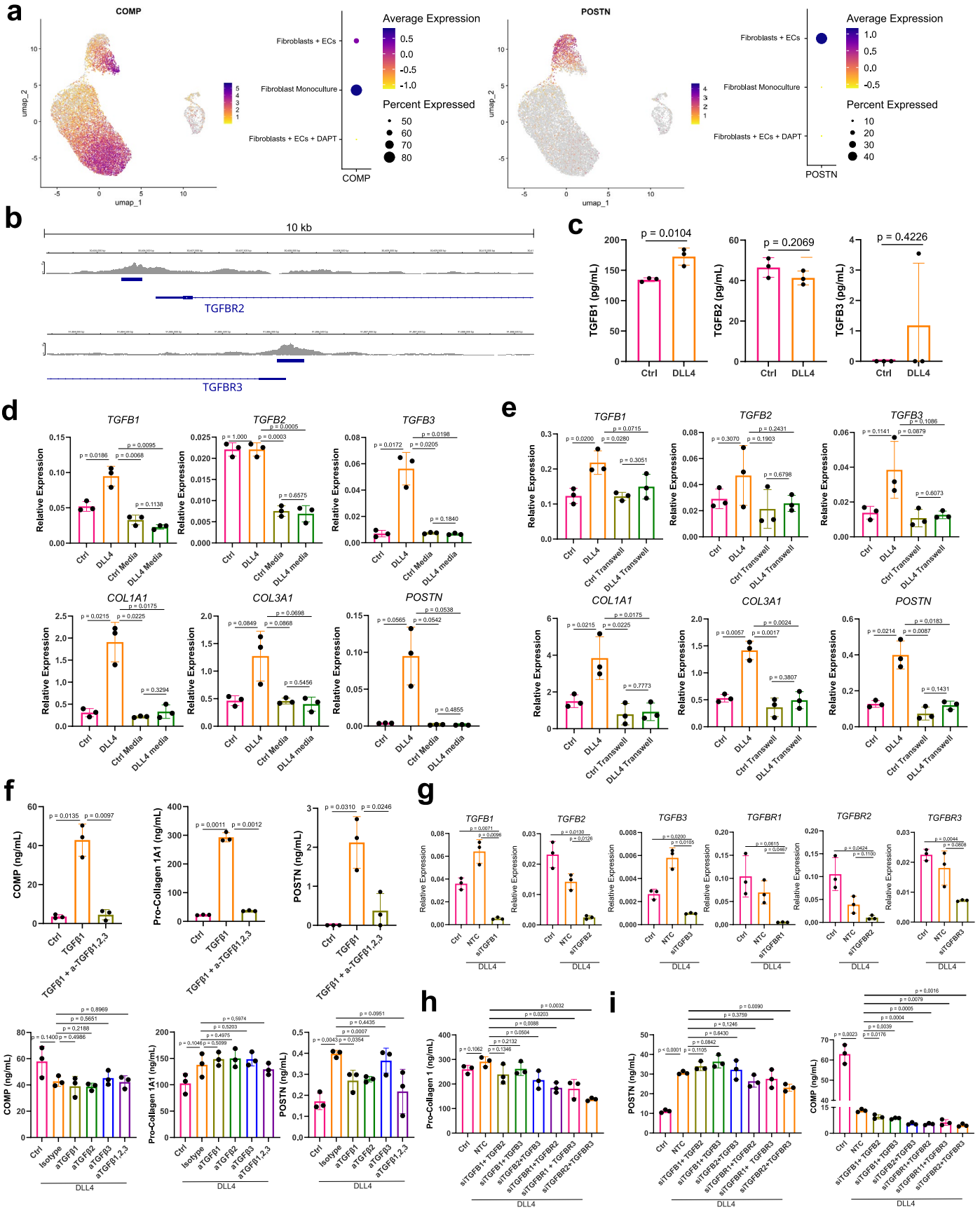

Extended Data Fig. 6 | See next page for caption.

https://doi.org/10.1038/s41590-025-02386-2

Extended Data Fig. 6 | Notch-mediated regulation of TGFβ signaling. a, UMAP projection and dotplots of single-cell 3D co-culture data displaying *COMP* and *POSTN* expression[9]. **b**, Chip-seq analysis of RBPJ binding to *TGFBR2* (-350 bp to -138 bp upstream of transcriptional start site (TSS)) and *TGFBR3* (-185 bp to +84 bp relative to TSS) promoter regions in HepG2 cells (data from GSE127388). Significant peaks are annotated with blue bars and were called using the narrowPeak function in MACS2. **c**, ELISA quantification of supernatant TGFβ1, TGFβ2, and TGFβ3 from fibroblasts stimulated with DLL4 for 3 days. **d**, RT-qPCR analysis of TGFβ isoform and fibrogenic gene expression in unstimulated or DLL4-stimulated fibroblasts (72 h) and fibroblasts that were exposed to conditioned media from unstimulated and DLL4-stimulated fibroblasts for 72 h. **e**, RT-qPCR analysis of TGFβ isoform and fibrogenic gene expression in unstimulated or DLL4-stimulated cells plated in the bottom chamber and fibroblasts that were cultured in the above transwell insert for 72 h. **f**, Top: ELISA quantification of supernatant COMP, PRO-COL1 and POSTN from fibroblasts stimulated with or without recombinant TGFβ1 (10 ng ml−1) and with or without a pan-TGFβ blocking antibody (5 ug mL-1) for 72 h. Below: ELISA quantification of COMP, PRO-COL1 and POSTN on unstimulated or DLL4-stimulated fibroblasts that were treated with antibodies against individual or pan-TGFβ isoforms (5 ug mL-1) for 72 h. **g**, RT-qPCR analysis of fibroblasts with or without DLL4 stimulation that were treated with siRNA (20 nM) for 96 h. **h-i**, ELISA quantification of fibroblast production of PRO-COL1, POSTN and COMP over 24 h after 72 h treatment with indicated siRNA combinations (10 nM each) with or without DLL4 stimulation. For **c-i** Data are shown as mean +/- s.d with n = 3 biological replicates, and representative of at least two independent experiments. Statistical analysis was performed by unpaired two-sided t-test.

https://doi.org/10.1038/s41590-025-02386-2

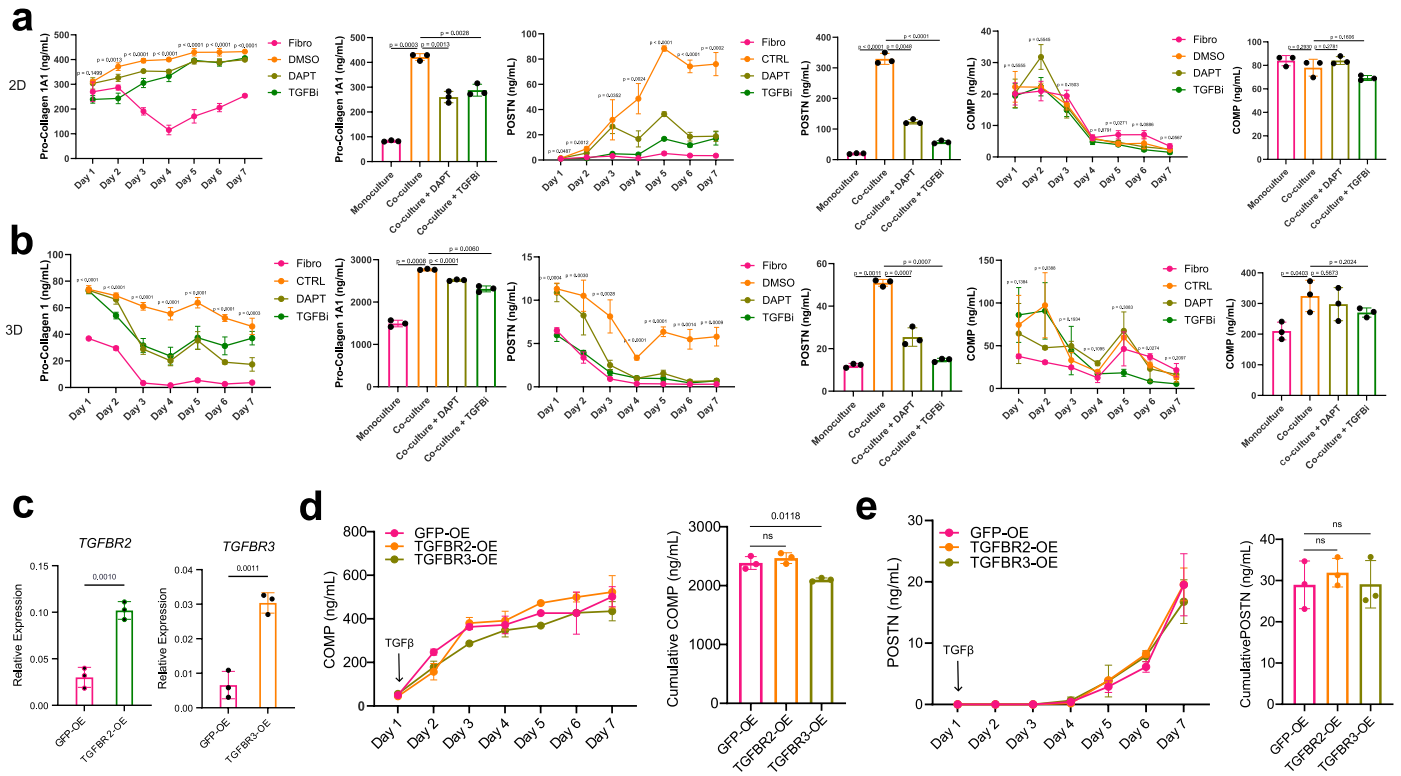

Extended Data Fig. 7 | Lentiviral overexpression of *TGFBR2* and *TGFBR3*. a-b, Monocultures of 5,000 fibroblasts (**a**, 2D culture) or 200,000 fibroblasts (**b**, 3D culture) or co-cultures of 5,000 fibroblasts with 5,000 HUVECs (**a**) or 100,000 fibroblasts and 100,000 HUVECs (**b**) were seeded with or without indicated inhibitors. ELISA quantification of POSTN, COMP and PRO-COL1 over the course of co-culture. *P*-values in the line graph are displayed for the comparisons between monoculture and co-culture without inhibitors (2D culture cumulative PRO-COL1: p = 0.0003, cumulative POSTN: p < 0.0001, cumulative COMP: p = 0.2930, 3D culture cumulative PRO-COL1: p = 0.0008, cumulative POSTN: p < 0.0011, cumulative COMP: p = 0.0403). The respective bar charts to the right represent the area under the curve. **c**, RT-qPCR analysis of *TGFBR2* and *TGFBR3* expression in *TGFBR2*-overexpressing or *TGFBR3*-overexpressing fibroblasts respectively, compared to control *GFP*-overexpressing fibroblasts. **d-e**, ELISA quantification of COMP and POSTN production from *GFP*-OE, *TGFBR2*-OE or *TGFBR3*-OE stimulated continuously with recombinant TGFβ1 (10 ng ml−1) stimulation. The bar plots to the right represent the area under the curve. For **a-e**, two-tailed unpaired t-test was used, represent n = 3 biological replicates, are shown as mean +/- s.d. and are representative of at least two independent experiments.

https://doi.org/10.1038/s41590-025-02386-2

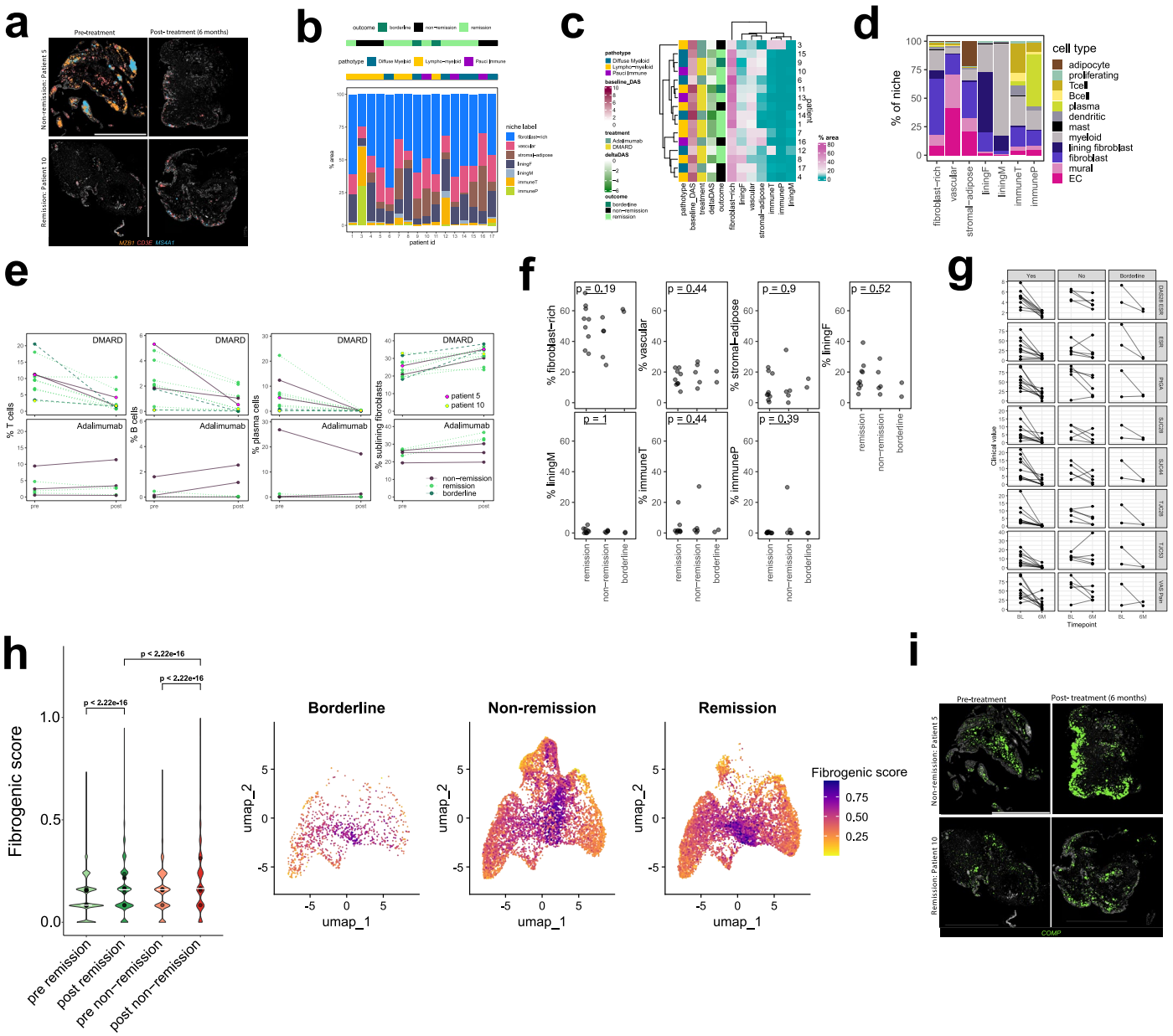

Extended Data Fig. 8 | Analysis of posttreatment biopsies. a, Representative pre- and post-treatment gene expression from remission (n = 10) and non-remission patients (n = 5). *MZB1* marks plasma cells, *CD3E* T cells and *MS4A1* B cells; scale bar indicates 2 mm. **b**, Stacked bar plot summarizing cell type proportion in post-treatment samples for 17 patients. **c**, Heat map representing the abundance of tissue niches, by tissue area, in each post-treatment biopsy and the associated clinical metadata. Baseline DAS and ΔDAS represent the DAS28-ESR pre-treatment and the change at 6-months, respectively. **d**, Stacked bar plot representing the proportion of cell types per niche post-treatment. **e**, Quantification of the relative abundance of immune cell types pre- and post-treatment. Line colors indicate remission status. Patient 5 is highlighted in magenta, and Patient 10 is highlighted in yellow. **f**, Jitter plot representing the tissue area of each niche in post-treatment biopsies by remission status. **g**, Line plots showing scores for pre- and post-treatment DAS components separated by remission status. **h**, Violin plot (left) and niche UMAP projection (right) displaying single cell fibrogenic UCell scores. Median values in violin plot represented by a white bar and median per patient values represented by points. p < 2.22e-16 for the comparison between indicated groups, two-sided Wilcoxon test. **i**, Representative examples of *COMP* transcript expression in pre and posttreatment synovial biopsies for a remission (n = 10) and non-remission patient (n = 5). **e**,**f** Statistics were calculated by two-sided Wilcoxon test.

https://doi.org/10.1038/s41590-025-02386-2

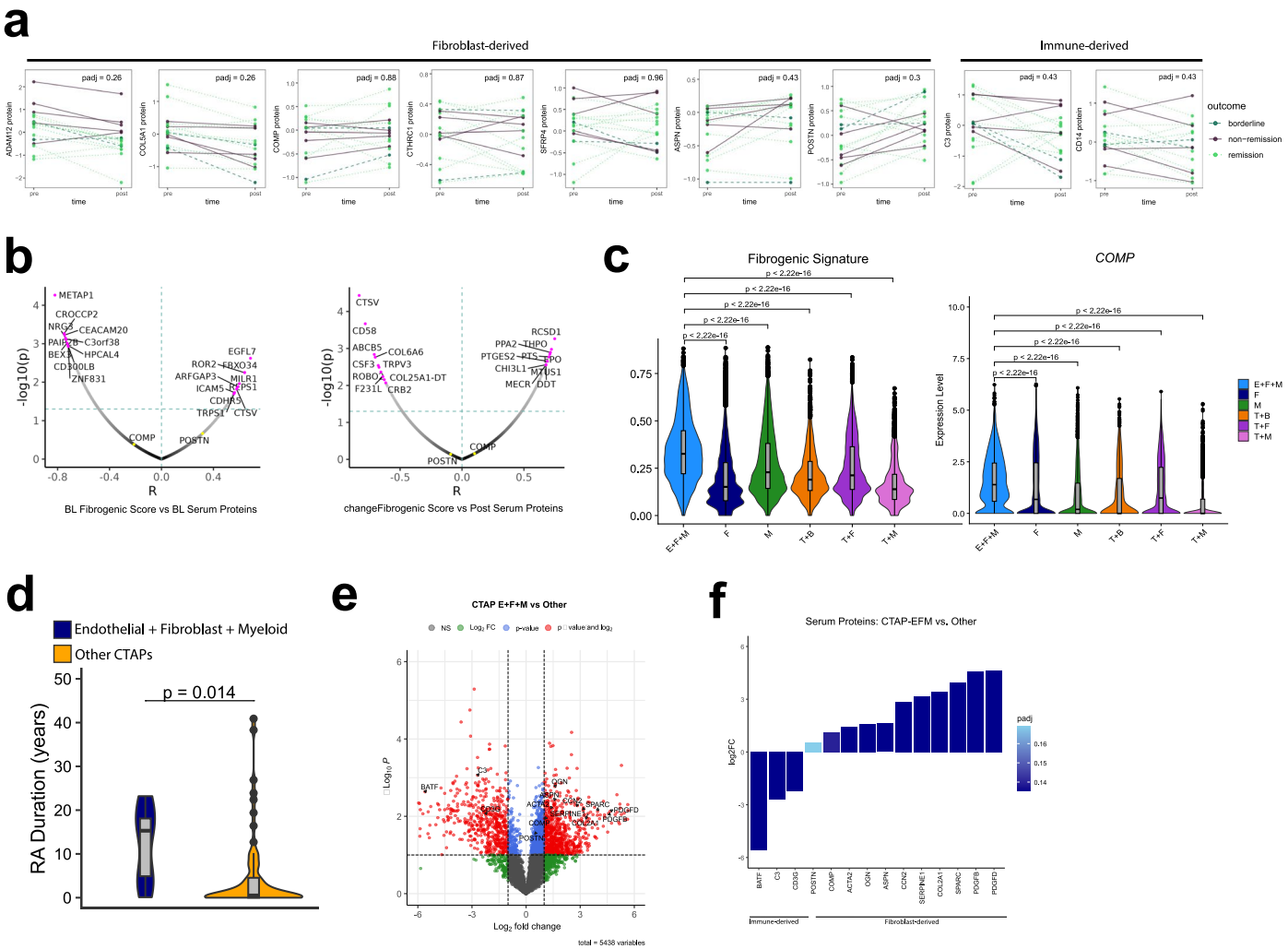

Extended Data Fig. 9 | RA serum protein analysis. a, Line plots showing pre- and post-treatment serum protein quantification of selected fibrogenic and immune markers reported as NPX values. A difference of 1 NPX signifies a doubling of protein. Statistics by two-sided Wilcoxon test, FDR corrected. **b**, Volcano plot showing the R-values and nominal p-values of baseline serum proteins correlated with baseline patient-level fibrogenic signature score (left) and posttreatment serum proteins with change in fibrogenic signature score (right) with the top 10 positively and negatively correlated genes indicated. Statistics by two-sided Pearson correlation coefficient test. **c**, Violin plot representing the distribution of fibrogenic gene signature score and *COMP* expression of synovial fibroblasts from each CTAP (EFM: n = 7, F: n = 11, M: n = 18, T + B: n = 14, T + F: n = 8, T + M: n = 12). Statistics by two-sided Wilcoxon test with Bonferroni correction. p < 2.22e-16 in the comparison between E + F + M and other CTAPs. **d**, Violin plot representing the distribution of disease duration in RA patients classified as CTAP-EFM (n = 7) versus RA patients classified as other CTAPs (n = 63). Statistics by two-sided Wilcoxon test. **e**, Volcano plot of differentially abundant serum proteins in CTAP-EFM patients compared to patients assigned to other CTAPs with selected genes highlighted. Differential expression was assessed with limma: linear models fitted per gene and empirical Bayes moderation of the standard errors to produce moderated t-statistics; p-values shown are unadjusted. **f**, Bar plot of selected serum proteins that are differentially abundant in RA patients classified as CTAP-EFM compared to RA patients classified as other CTAPs. The height of the bar represents the log-fold change, and the shading of the bar represents adjusted p-values with FDR correction. **c**,**d** the box plots show the median and 25th–75th percentiles; the whiskers represent 1.5 times the interquartile range (IQR); outliers are shown beyond the whiskers.

https://doi.org/10.1038/s41590-025-02386-2

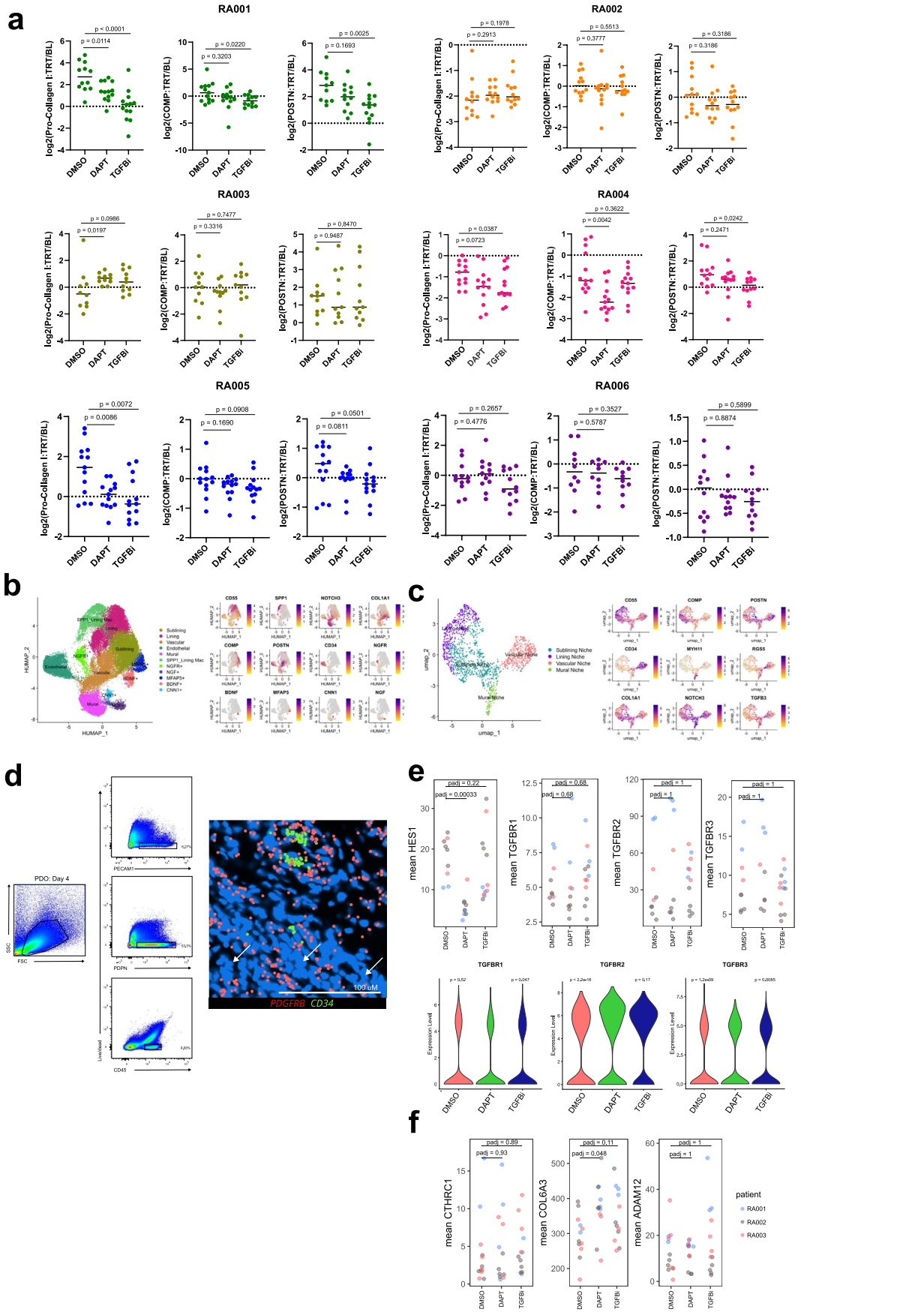

Extended Data Fig. 10 | See next page for caption.

https://doi.org/10.1038/s41590-025-02386-2

Extended Data Fig. 10 | Proteomic and spatial analysis of inhibitor-treated patient derived organoids. a, Jitter plots showing normalized per organoid (dot) ELISA quantification of indicated proteins. Log_2 fold change of measurements from 72 h treatment normalized to baseline measurements obtained after overnight incubation is shown (n = 6 patients, PDO replicates per treatment: RA001 n = 12, RA002 n = 12, RA003 n = 11, RA004 n = 13, RA005 n = 13, RA006 n = 12) **b**, UMAP projection of single cells detected in spatially profiled PDOs with individual marker genes shown (right). **c**, UMAP projection of Tessera-defined niches (left) and gene expression plots (right) showing niche-tile level gene expression. **d**, Representative flow gating strategy (left) with live cell type populations encircled and spatial plot (right) of a PDO with indicated transcripts. Scale bar is 100 µm. **e**, Jitter plot that indicates average mural cell expression, per-PDO, of indicated genes (top) and violin plot (bottom) that shows aggregated single-cell expression by condition. **f**, Jitter plot that indicates average fibroblast expression, per-PDO, of indicated gene. For **a** two-sided unpaired t-tests were used and for **e,f**, two-sided Wilcoxon test was used. Flow cytometry gating in **d** is representative of three independent experiments and three biological replicates.

nature portfolio

Corresponding author(s): Kevin Wei MD, PhD

Last updated by author(s): 11/20/2025

Reporting Summary

Nature Portfolio wishes to improve the reproducibility of the work that we publish. This form provides structure for consistency and transparency in reporting. For further information on Nature Portfolio policies, see our Editorial Policies and the Editorial Policy Checklist.

Statistics

For all statistical analyses, confirm that the following items are present in the figure legend, table legend, main text, or Methods section.

n/a	Confirmed
☐	☒ The exact sample size (*n*) for each experimental group/condition, given as a discrete number and unit of measurement
☐	☒ A statement on whether measurements were taken from distinct samples or whether the same sample was measured repeatedly
☐	☒ The statistical test(s) used AND whether they are one- or two-sided *Only common tests should be described solely by name; describe more complex techniques in the Methods section.*
☐	☒ A description of all covariates tested
☐	☒ A description of any assumptions or corrections, such as tests of normality and adjustment for multiple comparisons
☐	☒ A full description of the statistical parameters including central tendency (e.g. means) or other basic estimates (e.g. regression coefficient) AND variation (e.g. standard deviation) or associated estimates of uncertainty (e.g. confidence intervals)
☐	☒ For null hypothesis testing, the test statistic (e.g. *F*, *t*, *r*) with confidence intervals, effect sizes, degrees of freedom and *P* value noted *Give P values as exact values whenever suitable.*
☒	☐ For Bayesian analysis, information on the choice of priors and Markov chain Monte Carlo settings
☒	☐ For hierarchical and complex designs, identification of the appropriate level for tests and full reporting of outcomes
☐	☒ Estimates of effect sizes (e.g. Cohen's *d*, Pearson's *r*), indicating how they were calculated

Our web collection on statistics for biologists contains articles on many of the points above.

Software and code

Policy information about availability of computer code

Data collection	Xenium Analyzer instrument used for spatial transcriptomic data collection. BD FACSCanto II was used for flow cytometry data collection. EVOS M7000 was used for image acquisition. Bio-rad ChemiDoc used for western blot imaging. Spectramax M3 was used for absorbance readings.
Data analysis	FlowJo_v10.10.0, GraphPad Prism 10, ImageJ 1.54g, Xenium Explorer v3.2, Tessera (open source), Loupe v9.0. R (v4.4.1) was used with the following packages: Seurat v5.0, DESeq2 v3.2, Harmony v1.2.3, limma v3.20, eks v1.0.7

For manuscripts utilizing custom algorithms or software that are central to the research but not yet described in published literature, software must be made available to editors and reviewers. We strongly encourage code deposition in a community repository (e.g. GitHub). See the Nature Portfolio guidelines for submitting code & software for further information.

Data

Policy information about availability of data

All manuscripts must include a data availability statement. This statement should provide the following information, where applicable:

- Accession codes, unique identifiers, or web links for publicly available datasets
- A description of any restrictions on data availability
- For clinical datasets or third party data, please ensure that the statement adheres to our policy

Previously published publicly available data used in this study are available in the following repositories: systemic sclerosis single-cell RNA sequencing data

(GSE195452), idiopathic pulmonary fibrosis single-cell RNA sequencing data (GSE136831), synovial single-cell RNA sequencing data (https://doi.org/10.7303/syn52297840), micromass organoid single-cell RNA sequencing data (https://www.immport.org; SDY1599), PEAC data (E-MTAB-6141), RBPJ Chip-seq data (GSE127388; ENCSR596FEL). All spatial transcriptomic data generated as part of this study are available on Zenodo: RA synovial pre-treatment data: https://doi.org/10.5281/zenodo.15058262. RA synovial post-treatment data: https://doi.org/10.5281/zenodo.15058715. RA synovial custom fibrogenesis panel (n = 4 tissues) and AMP Olink matrix containing NPX values and clinical metadata: https://doi.org/10.5281/zenodo.15059437. Xenium profiling of 2D co-culture: https://doi.org/10.5281/zenodo.15064564. RA-ILD Lung and RA synovium Visum data, RA patient-derived organoid Xenium data, 3D co-culture Xenium Data, 396.10 Olink data: https://doi.org/10.5281/zenodo.16995699.

Research involving human participants, their data, or biological material

Policy information about studies with human participants or human data. See also policy information about sex, gender (identity/presentation), and sexual orientation and race, ethnicity and racism.

Reporting on sex and gender	The sexes of human participants has been reported in Supplementary Table 1. Sex was determined by self-reporting. Sex as a biological variable was not considered in this study.
Reporting on race, ethnicity, or other socially relevant groupings	Data about race or ethnicity was not collected or included as part of the study design or analyses.
Population characteristics	Population characteristics of the human participants is listed in Supplementary Table 1.
Recruitment	Synovium from patients with RA or OA were retrieved via biopsy, arthroplasty or synovectomy at Flinders Medical Centre, Brigham and Women's Hospital, University of Colorado Anschutz medical center and Hospital for Special Surgery. All participants were enrolled on a voluntary basis and provided written consent.
Ethics oversight	Southern Adelaide Clinical Human Research Ethics Committee (Protocol #396.10), the Mass General Brigham Human Research Committee (IRB 2019P002924), the Colorado Multiple Institutional Review Board (IRB 20-1908), and Hospital for Special Surgery (IRB 2014-233).

Note that full information on the approval of the study protocol must also be provided in the manuscript.

Field-specific reporting

Please select the one below that is the best fit for your research. If you are not sure, read the appropriate sections before making your selection.

☐ Life sciences ☐ Behavioural & social sciences ☐ Ecological, evolutionary & environmental sciences

For a reference copy of the document with all sections, see nature.com/documents/nr-reporting-summary-flat.pdf

Life sciences study design

All studies must disclose on these points even when the disclosure is negative.

Sample size	No statistical methods were used to determine sample size. For spatial transcriptomic data, sample size was determined based on contemporary spatial studies. For imaging analysis, sample size (number of cells quantified) was determined in order to robustly capture the distribution of cell phenotypes observed in vitro. For in vitro experiments, sample size was determined based on preliminary experiments and previous publications.
Data exclusions	Single-cell data derived from spatial transcriptomics was filtered to remove doublets and cells with low RNA as described in methods. Prior to data integration and niche analysis, one sample was excluded due to transcript sparsity.
Replication	For spatial transcriptomic data, the observations were validated across 2 independent patient cohorts, as described in the text. The reproducibility of all in vitro data was confirmed with at least two independent experiments.
Randomization	Paired pre- and post-treatment synovial samples from the same patient and same joint were run on the same spatial transcriptomic imaging slide in order to reduce potential batch effects. Randomization n/a for other aspects of the study.
Blinding	No blinding was performed as there was no intervention.

Behavioural & social sciences study design

All studies must disclose on these points even when the disclosure is negative.

Study description	*Briefly describe the study type including whether data are quantitative, qualitative, or mixed-methods (e.g. qualitative cross-sectional, quantitative experimental, mixed-methods case study).*
Research sample	*State the research sample (e.g. Harvard university undergraduates, villagers in rural India) and provide relevant demographic*

Research sample	*information (e.g. age, sex) and indicate whether the sample is representative. Provide a rationale for the study sample chosen. For studies involving existing datasets, please describe the dataset and source.*
Sampling strategy	*Describe the sampling procedure (e.g. random, snowball, stratified, convenience). Describe the statistical methods that were used to predetermine sample size OR if no sample-size calculation was performed, describe how sample sizes were chosen and provide a rationale for why these sample sizes are sufficient. For qualitative data, please indicate whether data saturation was considered, and what criteria were used to decide that no further sampling was needed.*
Data collection	*Provide details about the data collection procedure, including the instruments or devices used to record the data (e.g. pen and paper, computer, eye tracker, video or audio equipment) whether anyone was present besides the participant(s) and the researcher, and whether the researcher was blind to experimental condition and/or the study hypothesis during data collection.*
Timing	*Indicate the start and stop dates of data collection. If there is a gap between collection periods, state the dates for each sample cohort.*
Data exclusions	*If no data were excluded from the analyses, state so OR if data were excluded, provide the exact number of exclusions and the rationale behind them, indicating whether exclusion criteria were pre-established.*
Non-participation	*State how many participants dropped out/declined participation and the reason(s) given OR provide response rate OR state that no participants dropped out/declined participation.*
Randomization	*If participants were not allocated into experimental groups, state so OR describe how participants were allocated to groups, and if allocation was not random, describe how covariates were controlled.*

Ecological, evolutionary & environmental sciences study design

All studies must disclose on these points even when the disclosure is negative.

Study description	*Briefly describe the study. For quantitative data include treatment factors and interactions, design structure (e.g. factorial, nested, hierarchical), nature and number of experimental units and replicates.*
Research sample	*Describe the research sample (e.g. a group of tagged Passer domesticus, all Stenocereus thurberi within Organ Pipe Cactus National Monument), and provide a rationale for the sample choice. When relevant, describe the organism taxa, source, sex, age range and any manipulations. State what population the sample is meant to represent when applicable. For studies involving existing datasets, describe the data and its source.*
Sampling strategy	*Note the sampling procedure. Describe the statistical methods that were used to predetermine sample size OR if no sample-size calculation was performed, describe how sample sizes were chosen and provide a rationale for why these sample sizes are sufficient.*
Data collection	*Describe the data collection procedure, including who recorded the data and how.*
Timing and spatial scale	*Indicate the start and stop dates of data collection, noting the frequency and periodicity of sampling and providing a rationale for these choices. If there is a gap between collection periods, state the dates for each sample cohort. Specify the spatial scale from which the data are taken*
Data exclusions	*If no data were excluded from the analyses, state so OR if data were excluded, describe the exclusions and the rationale behind them, indicating whether exclusion criteria were pre-established.*
Reproducibility	*Describe the measures taken to verify the reproducibility of experimental findings. For each experiment, note whether any attempts to repeat the experiment failed OR state that all attempts to repeat the experiment were successful.*
Randomization	*Describe how samples/organisms/participants were allocated into groups. If allocation was not random, describe how covariates were controlled. If this is not relevant to your study, explain why.*
Blinding	*Describe the extent of blinding used during data acquisition and analysis. If blinding was not possible, describe why OR explain why blinding was not relevant to your study.*

Did the study involve field work? ☐ Yes ☐ No

Field work, collection and transport

Field conditions	*Describe the study conditions for field work, providing relevant parameters (e.g. temperature, rainfall).*
Location	*State the location of the sampling or experiment, providing relevant parameters (e.g. latitude and longitude, elevation, water depth).*
Access & import/export	*Describe the efforts you have made to access habitats and to collect and import/export your samples in a responsible manner and in compliance with local, national and international laws, noting any permits that were obtained (give the name of the issuing authority, the date of issue, and any identifying information).*

Disturbance | *Describe any disturbance caused by the study and how it was minimized.*

Reporting for specific materials, systems and methods

We require information from authors about some types of materials, experimental systems and methods used in many studies. Here, indicate whether each material, system or method listed is relevant to your study. If you are not sure if a list item applies to your research, read the appropriate section before selecting a response.

Materials & experimental systems

n/a	Involved in the study
☐	☒ Antibodies
☐	☒ Eukaryotic cell lines
☒	☐ Palaeontology and archaeology
☒	☐ Animals and other organisms
☒	☐ Clinical data
☒	☐ Dual use research of concern
☒	☐ Plants

Methods

n/a	Involved in the study
☒	☐ ChIP-seq
☐	☒ Flow cytometry
☒	☐ MRI-based neuroimaging

Antibodies

Antibodies used

Immunofluorescence : Phospho-SMAD3 (Ser423, Ser425) (16H5L12), Thermofisher Cat. 702292; TGF beta-1 (TB21), Thermofisher Cat. MA5-18023; TGF beta-2 (220ct16.4.3.1), Thermofisher Cat. MA5-37505; TGF beta-3, Thermofisher Cat. PA1-38736; PE anti-human Notch 3 (MHN3-21), Biolegend Cat. 345405; FITC anti-human CD45 (2D1), Biolegend Cat. 368507; Collagen I (COL-1), Thermofisher Cat. MA1-26771; VWF (F8/86), Thermofisher Cat. MA5-14029; Goat anti-Mouse IgG Alexa Fluor 660, Thermofisher Cat. A-21055; Donkey anti-Rabbit IgG Secondary Antibody Alexa Fluor 555, Thermofisher Cat. A-31572.

Flow Cytometry: APC anti-human TGF-β Receptor II, Biolgend Cat. 399705; TGFBR3, Thermofisher Cat. 20000-1-AP; FITC anti-human CD31 (WM59), Biolegend 303103. anti-Rabbit IgG Secondary Antibody Alexa Fluor 555, Thermofisher Cat. A-31572. BV421-CD31, Biolegend Cat. 303123, FITC-CD45 Biolegend Cat. 368507, PE-PDPN Biolegend Cat. 337003

Western Blot: TGF Beta 1, Proteintech Cat. 21898-1-AP; TGF Beta 2, Proteintech Cat. 19999-1-AP; TGF Beta 3, Proteintech Cat. 18942-1-AP; Human TGF-beta RI/ALK-5, R&D Systems Cat. AF3025; TGF beta Receptor 2, Bioss Cat. BS-0117R; TGF-β Receptor III, Cell Signaling Technology 2591S; GAPDH, Thermofisher Cat. MA5-15738

Validation

All antibodies used are commercially available and have been validated by the manufacturer. Validation data is available on the manufacturer's website.

Eukaryotic cell lines

Policy information about cell lines and Sex and Gender in Research

Cell line source(s)

Primary synovial fibroblast cell lines isolated from OA or RA patients were used. HUVECs were attained from Thermofisher (https://www.thermofisher.com/order/catalog/product/C0035C)

Authentication

None of the cell lines were authenticated

Mycoplasma contamination

Cells lines were not tested for mycoplasma.

Commonly misidentified lines
(See ICLAC register)

Not applicable

Plants

Seed stocks

Report on the source of all seed stocks or other plant material used. If applicable, state the seed stock centre and catalogue number. If plant specimens were collected from the field, describe the collection location, date and sampling procedures.

Novel plant genotypes

Describe the methods by which all novel plant genotypes were produced. This includes those generated by transgenic approaches, gene editing, chemical/radiation-based mutagenesis and hybridization. For transgenic lines, describe the transformation method, the number of independent lines analyzed and the generation upon which experiments were performed. For gene-edited lines, describe the editor used, the endogenous sequence targeted for editing, the targeting guide RNA sequence (if applicable) and how the editor was applied.

Authentication

Describe any authentication procedures for each seed stock used or novel genotype generated. Describe any experiments used to assess the effect of a mutation and, where applicable, how potential secondary effects (e.g. second site T-DNA insertions, mosiacism, off-target gene editing) were examined.

Flow Cytometry

Plots

Confirm that:

☒ The axis labels state the marker and fluorochrome used (e.g. CD4-FITC).

☒ The axis scales are clearly visible. Include numbers along axes only for bottom left plot of group (a 'group' is an analysis of identical markers).

☒ All plots are contour plots with outliers or pseudocolor plots.

☒ A numerical value for number of cells or percentage (with statistics) is provided.

Methodology

Sample preparation	Fibroblasts or co-culture of fibroblasts and endothelial cells were trypsinized and directly stained with an equal volume of primary antibody solution (Cell staining buffer, Biolegend) containing eFluor 780 Fixable Viability Dye (Thermofisher, 1:1000), TGFBR2-APC (Biolegend, 1:100), TGFBR3 (Proteintech, 20000-1-AP, 1:100) or CD31-FITC (Biolegend, 1:100) for 30 minutes at 4C. Cells were washed with cell staining buffer (Biolegend), fixed in 4% PFA for 10 minutes at RT, washed, and stained with AF555 anti-rabbit (Thermofisher) for 30 minutes at 4°C for detection of TGFBR3. Cells were washed and resuspended in cell staining buffer.
Instrument	BD FACSCanto II
Software	BD FACSDiva and Flowjo v10.10.0
Cell population abundance	Cells were not sorted prior to flow cytometry or experiments
Gating strategy	Fibroblasts gating: FSC-A/SSC-A plots were used to determine cell population gates. FSC-A/FSC-H plots were then used to determine singlet gates. Cells that were negative for the live/dead stain and negative for CD31 were selected for analysis.

☐ Tick this box to confirm that a figure exemplifying the gating strategy is provided in the Supplementary Information.